minerals

MDPI

Article

Chromite Oxidation Patterns Associated to Serpentinization: Case Studies from the Mid-Atlantic Ridge, the Alter do Chão Massif (NE Alentejo, Portugal) and the Ronda Massif (Spain)

Isabel Ribeiro da Costa [1,*] and Fernando J. A. S. Barriga [1,2]

[1] Departamento de Geologia, Faculdade de Ciências, Universidade de Lisboa, 1749-016 Lisbon, Portugal
[2] Instituto Dom Luiz (IDL), Faculdade de Ciências da Universidade de Lisboa, 1749-016 Lisbon, Portugal
* Correspondence: imscosta@fc.ul.pt

Abstract: Chromite oxidation during serpentinization of host peridotites is a well-documented process. Detailed compositional characterization of chromites and Cr-rich spinels from three geotectonic settings provided the basis for this study, focused on the comparison of their oxidation patterns as a means to evaluate the relative mobility of spinel components during serpentinization-related oxidation in those different contexts, namely: (*i*) tectonic exposures of serpentinized oceanic upper-mantle in the Azores sector of the Mid-Atlantic Ridge (MAR); (*ii*) serpentinized peridotites from Cabeço de Vide (CV, Alter do Chão Massif, Portugal); and (*iii*) serpentinized subcontinental mantle peridotites from the Ronda Massif (Spain). Electron microprobe data show that: (*i*) irrespective of geotectonic setting and original composition, Cr-spinels follow similar oxidation trends; (*ii*) early Cr-spinel oxidation, involving significant Mg- and Al-depletion leading to the formation of ferritchromit rims, has been more intense in the CV serpentinites than in the more recent MAR and Ronda serpentinites; (*iii*) with the possible exception of Zn, trace components (Mn, Ti, V, Ni and Co) seem to be relatively immobile during spinel oxidation, thus becoming slightly enriched in ferritchromit rims; (*iv*) extreme Cr-spinel oxidation is responsible for incomplete outer rims of magnetite on several grains. Time, fluid pH, and fluid/rock ratios seem to be the main factors controlling the intensity and extension of chromite oxidation.

Keywords: chromite oxidation; ferritchromit; serpentinization; Mid-Atlantic Ridge; Cabeço de Vide; Ronda

Citation: Ribeiro da Costa, I.; Barriga, F.J.A.S. Chromite Oxidation Patterns Associated to Serpentinization: Case Studies from the Mid-Atlantic Ridge, the Alter do Chão Massif (NE Alentejo, Portugal) and the Ronda Massif (Spain). *Minerals* **2022**, *12*, 1300. https://doi.org/10.3390/min12101300

Academic Editors: Adalene Moreira Silva, Catarina Labouré Bemfica Toledo and António Manuel Nunes Mateus

Received: 10 August 2022
Accepted: 11 October 2022
Published: 15 October 2022

1. Introduction

The minerals of the oxyspinel group (spinel supergroup) are characterized by a general AB_2O_4 formula, where A refers to the tetrahedral position, preferentially occupied by divalent transition metal cations (Mg, Fe^{2+}, Mn^{2+}, ±Zn, Ni, Co), and B refers to the octahedral site, which is mainly occupied by trivalent transition metal cations (Al, Cr, Fe^{3+}, ±Ti, V) [1,2]. In magnesiochromites and chromites, Cr is the main cation in the B position, whereas in chromian spinels, Al predominates in that position [1,2]. The term "chromite" has often been used in the text in a general sense, to include the three populations of Cr-rich oxyspinels that were the object of this study. The designation "ferritchromit", following its original definition, is used specifically to refer to F^{3+}-enriched chromite resulting from alteration (oxidation) of primary chromites, so the name has both a compositional and a genetic meaning.

Chromites or chromian spinels are common accessories in peridotitic rocks, and their oxidation during serpentinization of peridotites, with formation of ferritchromit (±magnetite) rims on primary chromite grains, due to gradual oxidation of Fe^{2+} to Fe^{3+} and intense Mg, Al, and eventually, Cr, depletion, has been extensively documented for a great number of occurrences [3–12]. The amount of magnetite produced as a result of

extreme oxidation of chromite is usually insignificant when compared with the secondary magnetite which results from serpentinization of olivine (±pyroxene) in these rocks.

Most of these studies have also discussed the origin of the ferritchromit (±magnetite) rims either as products of chromite alteration or overgrowths on the original chromite, taking into account both the solid-state diffusion rates of Mg, Al, Fe and Cr, and their solubilities under various pH conditions [3,4]. To the extent of our knowledge, however, studies on how chromite oxidation rate controls elemental variation rates in different serpentinization contexts and under the interaction of chemically different fluids have not been published yet. To evaluate such differences has been the focus of the present study, based on analytical data collected for chromite-ferritchromit pairs in serpentinites from three different geotectonic settings, namely the Azores sector of the Mid-Atlantic Ridge (MAR), the Alter do Chão mafic-ultramafic massif (NE Alentejo, Portugal), and the Ronda peridotite massif (SW Spain), and on the available information in the literature concerning the serpentinizing fluids in each case.

Previous studies on the MAR serpentinites [13–15] and detailed petrography of the Alter do Chão and Ronda serpentinites indicate that relic chromite is ubiquitous and some relic olivine (more rarely orthopyroxene) can still be recognized in some of these rocks, irrespective of their degree of serpentinization or dominant serpentine texture.

Detailed mineralogical data for a considerable number of chromite and Cr-rich spinel grains (a total of 93 grains) from serpentinites collected in these three settings are presented and discussed below. Special emphasis is given to the comparative discussion of the relative mobility of the main chemical components of chromite, during its oxidation, and of how fluid composition and fluid/rock ratios may condition chromite oxidation in each setting.

The preliminary conclusions of this study, concerning the way that fluid chemistry and physical parameters control the relative mobility patterns of chromite components during serpentinization of its host-rock, may be useful pathfinders not only in future studies concerning serpentinization of chromite-bearing ultramafic rocks, but also in exploration studies of ultramafic-hosted ores.

2. Serpentinization Settings

Three sets of chromite-bearing serpentinized peridotites from different geological contexts were used in the present study. Their respective geotectonic settings are described below.

The larger peridotite set corresponds to chromite-bearing harzburgite from the Rainbow hydrothermal field (36°14′ N) [16–19] and from the Saldanha site (36°34′ N) [20–23], in the Azores sector of the MAR (Figure 1a). These two sites are located on second-order ridge segments linked by left-lateral non-transform discontinuities, under the thermal and chemical influence of the Azores hotspot [16]. This setting favours deep seawater circulation and provides evidence of recent serpentinization and subsequent tectonic uplift and exposure of the serpentinized upper mantle ultramafics onto the seafloor, a recurrent feature on the MAR and other slow-spreading ridges characterized by limited melt production and long-term tectonic extension [22,24–30]. Previous mineralogical and isotopic studies on these MAR serpentinites indicate that: (i) serpentinization has taken place at temperatures as low as 300–200 °C; (ii) besides substantial bulk-rock hydration and some major component loss, serpentinization also involves significant oxidation, with a drastic increase in whole-rock $Fe_2O_3/(FeO + Fe_2O_3)$ ratios, which can sometimes exceed 0.75 [13,15].

The CV chromite set was sampled in serpentinized dunites and harzburgites from Cabeço de Vide, on the SW edge of the Alter do Chão Mafic-Ultramafic Massif, NE Alentejo (Portugal; Figure 1b). The Alter do Chão pluton consists of gabbroic rocks and serpentinized peridotites, and intrudes the thick Elvas Cambrian carbonate sequence, producing an intense metamorphic aureole along the contact zone [31]. The gabbroic rocks are probably older than ultramafic rocks and correspond to more than one intrusive event. The ultramafic rocks include peridotites, dunites and pyroxenites, exhibiting variable degrees of serpentinization [31–34]. Although the pluton and its host rocks have been subjected to the large-scale effects of the low- to intermediate-grade hercynian metamorphism, as well

as to several metasomatic effects (serpentinization, amphibolitization, scapolitization), the CV serpentinites and partially serpentinized peridotites show no clear signs of plastic deformation or post-serpentinization metamorphism on thin-section; olivine fracturing, on the other hand, has been intense and has very probably enhanced water circulation and serpentinization of these peridotites.

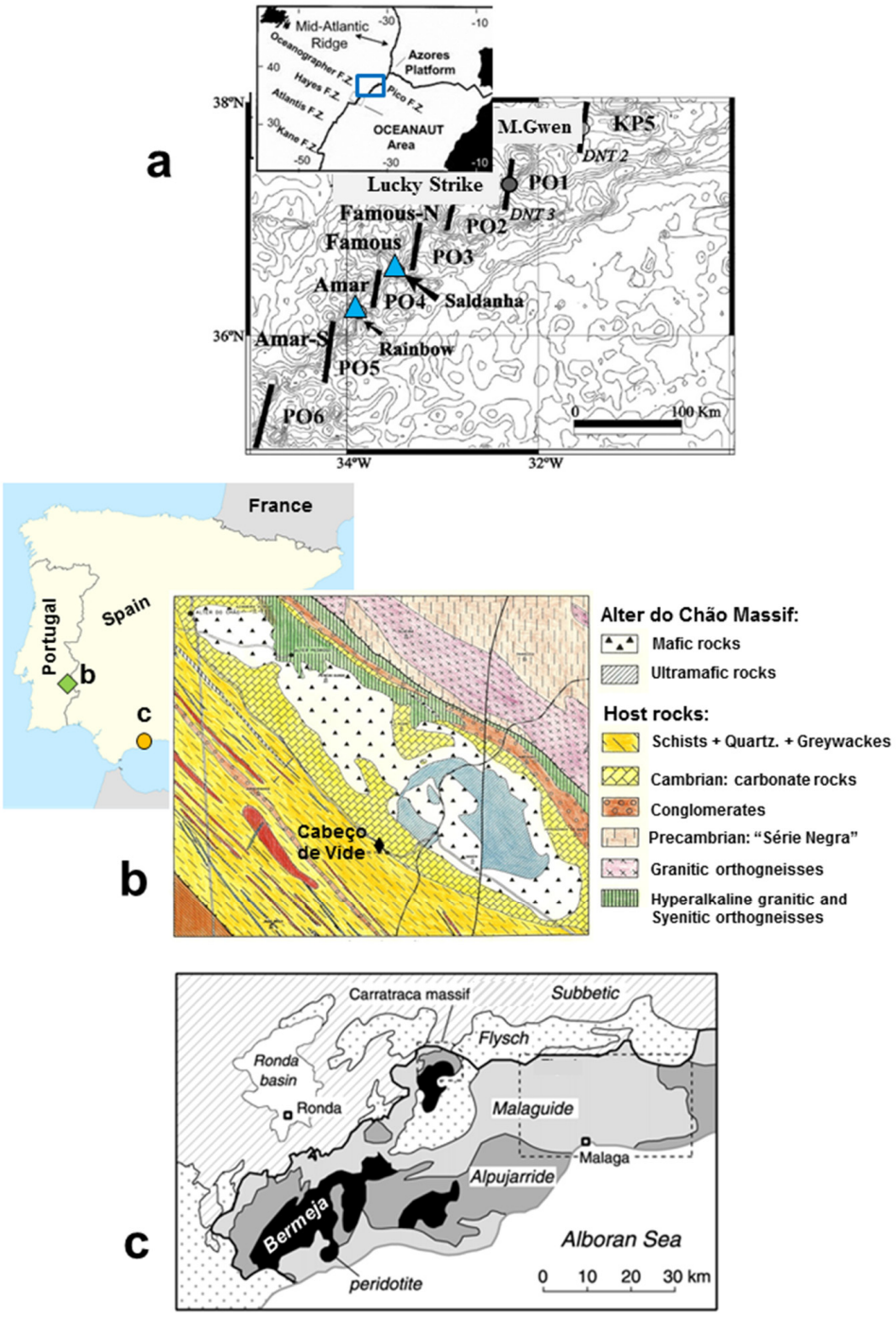

Figure 1. Location of the studied settings: (**a**) the Rainbow and Saldanha hydrothermal sites, in the Azores sector of the Mid-Atlantic Ridge [18,20]; (**b**) AC1 and AC2 boreholes (drilled by A. Cavaco Co.), in the Cabeço de Vide village, in the Alter do Chão mafic-ultramafic massif, NE Alentejo, Portugal (adapted from [31]); (**c**) the Bermeja Formation of the Ronda Massif in the Betic Cordillera, SW Spain (adapted from [35]).

In the serpentinized peridotites of Alter do Chão, pseudomorphic textures predominate, probably due to lower water/rock ratios and/or more limited tectonic deformation than those at which MAR serpentinization takes place. The CV serpentinites also show drastic overall oxidation, with most $Fe_2O_3/(FeO + Fe_2O_3)$ ratios in the 0.57–0.81 range (Ribeiro da Costa, *unpubl. data*).

The Ronda Peridotite Massif (SW Spain; Figure 1c) occurs within the greenschist- to granulite-facies metapelitic rocks of the Alpujárride Complex, on the western part of the Betic Cordillera, which forms the western end of the European Alpine Belt (e.g., [35,36]). Given their tectonic setting, the Ronda peridotites have been classified as alpine-type orogenic peridotites [37,38], and correspond to the crustal emplacement of large bodies of subcontinental mantle peridotites [38–40].

The Ronda peridotites, mostly plagioclase-bearing spinel lherzolites, harzburgites and dunites, form the lower part of the Los Reales Nappe and outcrop in several massifs, the largest and better preserved being those of Sierra Bermeja and Sierra Alpujata. These peridotites are estimated to have formed at initial high-P/high-T conditions (20–25 kbar, 1100–1200 °C), evolving towards low-P with little decrease in temperature (12–15 kbar to 5–7 kbar, 800–900 °C; [41,42]).

The Ronda peridotites form up to 2 km-thick allochthonous lenses [43–48], and serpentinization of these peridotites is associated to the late deformation episodes which affected this sector of the Betic Cordilleras. Exhumation of the Ronda peridotites has probably started between the Jurassic to the early Cretaceous, with lithosphere thinning and uplift of a hot asthenospheric mantle diapir related to the lateral displacement of Africa relative to Iberia. Convergence and collision between the two plates, with subduction of a continental lithosphere wedge, have prolonged the exhumation of these rocks to the present time [41–49]. Both transpression [49], alternating contractive and extensional processes [47], and pure extension [50] have been invoked to explain the late exhumation of subcontinental mantle in the Ronda area in the context of a large-scale Paleogene decompression event in the Western Mediterranean, though the final Miocene exhumation of Ronda Peridotite is probably associated to early folding and late shearing of the SCLM (subcontinental lithospheric mantle) in a compressive geodynamic setting [51,52].

The Ronda peridotites have kept the structures formed during the various stages of their exhumation process and are relatively unaltered, except those in contact with the metamorphic rocks or along late faults, where serpentinization has taken place. Three ultramafic facies occur in the Sierra Bermeja massif, all of them bearing accessory Cr-rich spinel [42]: garnet-bearing lherzolites, in the NW; spinel-bearing lherzolites in the western sector, to the south of the former facies; and plagioclase-bearing lherzolites, in the eastern sector.

3. Materials and Methods

The Rainbow and Saldanha samples were collected in situ, by submersible, at depths of approx. 2300–2200 m, during the FLORES (1996; 9 samples, ref. FL-) and SALDANHA (1998; 13 samples, ref. SAL-) oceanographic cruises (Figure 1a; Table 1).

The Alter do Chão samples were recovered from two nearly vertical boreholes (AC1 and AC2) drilled by the A. Cavaco Exploration Company near the Cabeço de Vide village and thermal springs, close to the contact between serpentinized peridotite and carbonate host-rocks (Figure 1b; Table 1). In the AC1 drill-core, serpentinites were sampled at depths between 180 and 190 m (2 samples), whereas they occupy a much thicker portion of drill-core AC2, between depths of 30 and 120 m (8 samples). Specific depths for each sample under study are given in Table 1. In both drill-cores, the serpentinized peridotites are overlain by recrystallized carbonate rocks.

Five samples from the Ronda Massif were collected during a guided field trip, at several locations of the Bermeja Formation (Figure 1c; Table 1), especially on the spinel-bearing lherzolites/harzburgites of the western sector.

The three chromite sets (Table 1) were labelled as follows: MAR (magnesiochromites from the Mid-Atlantic Ridge serpentinites), CV (chromites from the Cabeço de Vide drill-cores, Alter do Chão Massif, Portugal), and Ronda (Cr-rich spinels from the Ronda Massif, SW Spain).

Table 1. Sample distribution according to predominant serpentine textural features.

Predominant Textural Features	Location and Sample References
Partly serpentinized peridotites	**Ronda**: (R-1), R-2, R-5
Pseudomorphic serpentinites	**MAR**: FL-02-02B, FL-02-03, FL-02-04, FL-08-04 **CV**: AC1-1 (186 m), AC1-5 (182 m) **Ronda**: R-0, R-4
Recrystallized-mesh serpentinites	**MAR**: FL-07-03, FL-10-10, FL-10-15, SAL-07-02A SAL-07-04, SAL-07-05A, SAL-09-05A, SAL-09-11 **CV**: AC2-10 (69 m), AC2-13 (71 m), AC2-14 (83 m) **Ronda**: R-1
Recrystallized mesh + non-pseudomorphic serpentinites	**MAR**: SAL-07-01A, SAL-09-01, SAL-09-06 **CV**: AC2-7 (38 m), AC2-8 (50 m), AC2-16 (101 m), AC2-17 (107 m)
Non-pseudomorphic serpentinites	**MAR**: FL-08-05, FL-08-11, SAL-09-02A, SAL-09-02B, SAL-09-03A, SAL-09-04, SAL-09-05B **CV**: AC2-15 (86 m)

Electron microprobe (EMP) analyses of chromites from the MAR serpentinites were obtained on a JEOL JCXA-733, at the Centre of Geology (Geology Department, Faculty of Science, Lisbon University, Lisboa, Portugal). This EMP equipment operated at an accelerating voltage of 15 kV, with a standard beam diameter of 5 μm. Measuring times were 20 s on the analytical peak, and 5 s on each background. Mineral standards: spinel (Al and Mg), magnetite (Fe), chromite (Cr), ilmenite (Ti), $MnTiO_3$ (Mn, Ti), sphalerite (Zn), Ni-metal (Ni), Cu-metal (Cu) and Co-metal (Co). Chromites and Cr-rich spinels from the CV and Ronda serpentinites were analysed on a JEOL JXA-8500 electron microprobe, at the LNEG–Laboratório Nacional de Energia e Geologia facilities, at S. Mamede de Infesta, Porto, Portugal. The microprobe was operated at 15 kV and 10 nA, using a beam diameter of 3–5 μm. Measuring times were 20 s on the analytical peak, and 5 s on each background. The following mineral standards were used: almandine (Al), V-metal (V), $MnSiO_3$ (Mn), $MnTiO_3$ (Ti), Mg-olivine (Mg), Cr_2O_3 (Cr), Fe_2O_3 (Fe). In both cases, detection limits for the analysed elements were: 222 ppm (for Mg), 230 ppm (for Al, V, Co and Zn), 261 ppm (for Mn), 304 ppm (for Ti) and 358 ppm (for Fe and Cr).

Back-scattered electron (BSE) images and X-ray profiles for Mg, Cr, Al and Fe in three representative grains of the studied populations were obtained on a JEOL JXA-8200 EMP equipment, at the facilities of the Geology Department of Lisbon University, Lisboa, Portugal, using an accelerating voltage of 15 kV and a beam current of 27 nA; analysing crystals used for the X-ray profiles were TAP (for Mg and Al) and LiFH (for Cr and Fe).

Structural formulae of chromite and magnetite (based on the general spinel formula: $A^{2+}B^{3+}{}_2O_4$) were determined on a basis of 4 oxygen atoms per formula unit and assuming that trivalent cation (B) positions were fully occupied, thus yielding an ideal distribution of Fe^{3+} and Fe^{2+} in the structure, for a given total iron composition: the method implies an iterative process, until both conditions are met. Very good convergence was obtained for chromites after 4 or 5 iterations, and for magnetites at the 6th iteration. This method, developed by Figueiras and Mateus [53] and confirmed by Mössbauer spectroscopic studies [54], yields very similar values to those obtained assuming balanced spinels with $RO/R_2O_3 = 1$ [2], with the added advantage of enabling detection of vacant octahedral positions.

Serpentinization-related volume changes were estimated in a few MAR and CV serpentinites, by applying the Gresens' mass balance method [55] to olivine–mesh serpentine and orthopyrxene–bastite serpentine pairs, assuming a net gain of H_2O during serpentinization of both olivine and orthopyroxene, and considering the modal proportion of olivine + mesh serpentine and orthopyroxene + bastite serpentine in those rocks [15].

4. Results

4.1. Petrographic Features

Besides some occasional relic olivine and pyroxene, MAR, CV and Ronda serpentinites contain ubiquitous relics of primary chromite or Cr-rich spinel, which were the starting point for this comparative study.

Table 1 displays the sampling location, sample references and the main textural features of the studied serpentinites.

Primary chromite is ubiquitous in the sampled MAR serpentinites (0.1–3.1 modal%), unlike the rare olivine (Fo_{87-92}; <5 modal%) or orthopyroxene (En_{89-92}; <2.5 modal%) relics which occur only in a few Rainbow samples [15,55]. MAR chromites are anhedral, occasionally displaying "atoll" shapes (Figure 2a), and their grain size is quite variable ($\leq$0.03–2.4 mm), though dimensions > 0.2 mm predominate. Most chromite grains are translucent, exhibiting strong orange-brown or reddish-orange hues and a distinct opaque rim, as well as an opaque edge along their fractures. Back-scattered electron (BSE) images and X-ray profiles carried out on some grains confirm the abrupt compositional changes responsible for the development of such opaque rims surrounding homogeneous chromite cores and bordering chromite fractures.

Relic chromite is a ubiquitous accessory mineral in the intensely serpentinized CV peridotites, whereas relic ilmenite, rutile, sphene, pentlandite and Fe-Ni-Co-sulphides are much less abundant. Although the CV serpentinites also exhibit a wide range of pseudomorphic to more evolved non-pseudomorphic serpentine textures (Table 1), variably recrystallized pseudomorphic textures after olivine are largely dominant, implying the original peridotites in this area were essentially dunites. When present, relic silicates (olivine or olivine and orthopyroxene) make up less than 5 modal% of these rocks.

Chromites in the CV serpentinites are also anhedral, with variable grain size (0.1–1.4 mm; Figure 2b), but are opaque, so ferritchromitic rims were only detected on backscattered-electron images, or X-ray profiles.

The degree of serpentinization is quite variable in the Ronda samples, from R-1 and R-4 (with 5–10 modal% of relic olivine and orthopyroxene) and R-0 (~25% of relic silicates) to R-2 and R-5 (with <10% serpentine, against 80% olivine and ~5% orthopyroxene). Relic chromite grains in the sampled Ronda serpentinized peridotites and serpentinites (Table 1) are usually relatively small (<0.2–1.5 mm), irregular and variably fractured. Most grains exhibit brown or orange-brown colour, and present opaque ferritchromit or magnetite margins and rims along fractures (Figure 2c).

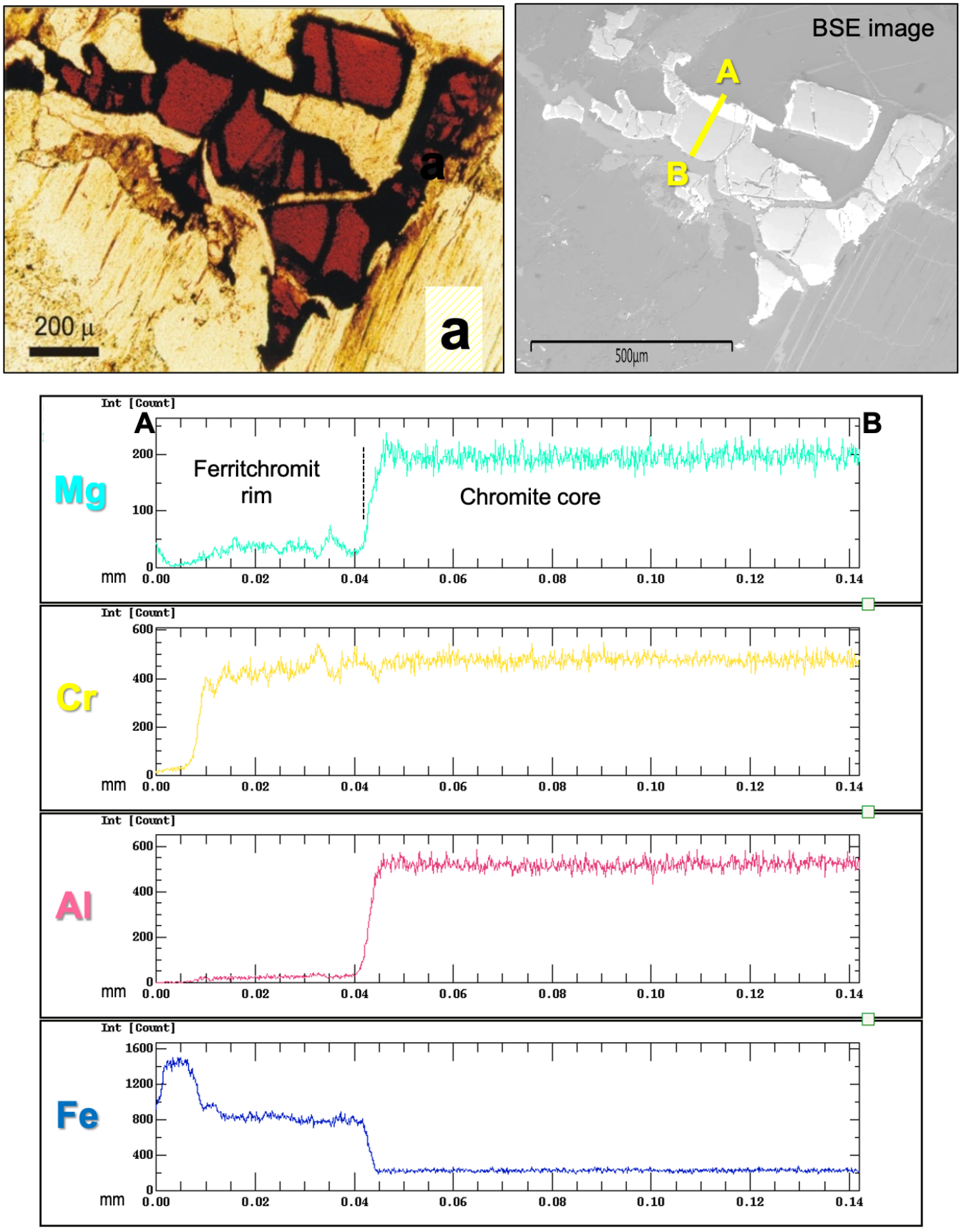

Figure 2. *Cont.*

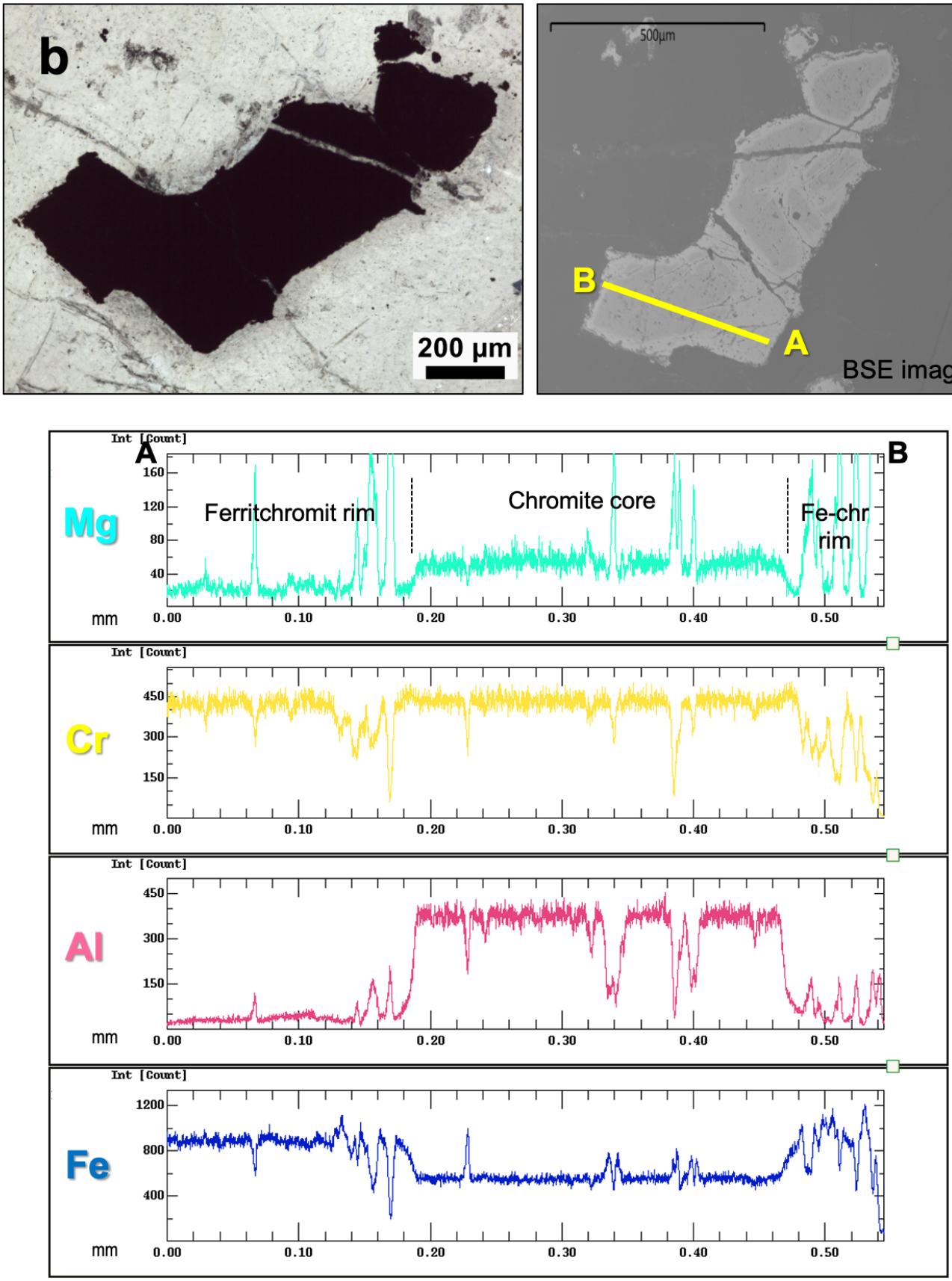

Figure 2. *Cont.*

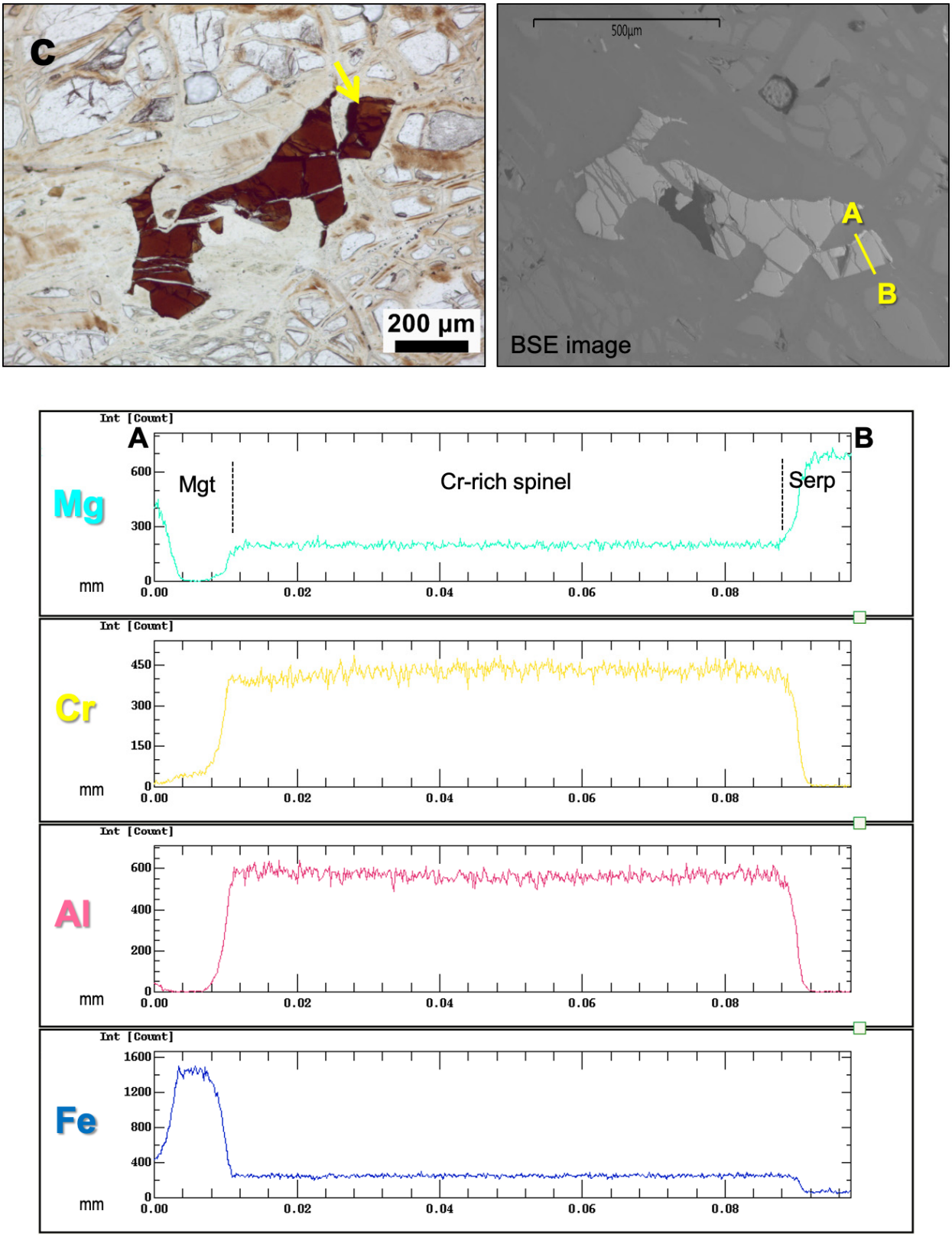

Figure 2. Transmitted-light photomicrographs, BSE images and X-ray profiles for the major components of relic chromite grains in the studied serpentinites: (**a**) well-developed opaque ferritchromit rims in anhedral chromite grains (sample FL-02-04, MAR; // pol.), with corresponding BSE image and X-ray profile on a cross-section (AB) from the wide ferritchromit rim through the homogeneous

chromite core. (**b**) opaque relic chromite grain enveloped by slightly recrystallized mesh serpentine in CV serpentinite (sample AC2-15; // pol.), with corresponding BSE image and X-ray profile on a cross-section (AB) including the wide ferritchromit rim through the homogeneous chromite core, and some enveloping serpentine on the B end; the Mg highs and Cr, Al and Fe lows observed within the core section correspond to serpentine filling thin microcracks in the chromite grain. (**c**) relic chromian spinel grain with thin partial magnetite rims (as that indicated by the yellow arrow), enveloped by mesh serpentine and relic olivine, in partly serpentinized peridotite from Ronda (sample R-2; // pol.), with corresponding BSE image and X-ray profile on a cross-section (AB) from the thin magnetite rim through a chromian spinel fragment.

4.2. Composition of Relic Chromites

EMP data, supported by transmitted-light petrography, backscattered-electron (BSE) imaging and X-ray profiles obtained on chromite grains from each setting (Figure 2), have revealed rather consistent oxidation patterns in the MAR, CV and Ronda spinels: most grains exhibit a homogeneous core and a narrow, continuous rim of ferritchromit, or close to ferritchromit composition (more rarely magnetite), which may also be present along fractures.

Representative and average chromite core-rim EMP data and structural formulae for MAR and CV chromites and Ronda Cr-rich spinels are given in Table A1 (Appendix A), and Table S1 (Supplementary Materials) includes the complete EMP data obtained for the three chromite sets.

From the compositional point of view, MAR and CV relic spinels can be classified as magnesiochromites and chromites, respectively, whereas the Ronda set corresponds to chromian spinels (Table A1, Figure 3). Some important distinctions between the three chromite sets are also immediately apparent: the cores of MAR magnesiochromites are richer in Mg than the CV cores; Cr < Al in the Ronda chromian spinel cores (Figures 3 and 4a); and, with few exceptions, the Fe^{3+} contents in primary cores of MAR magnesiochromites and Ronda chromian spinels are insignificant compared to those shown by most CV chromite cores (Figure 4).

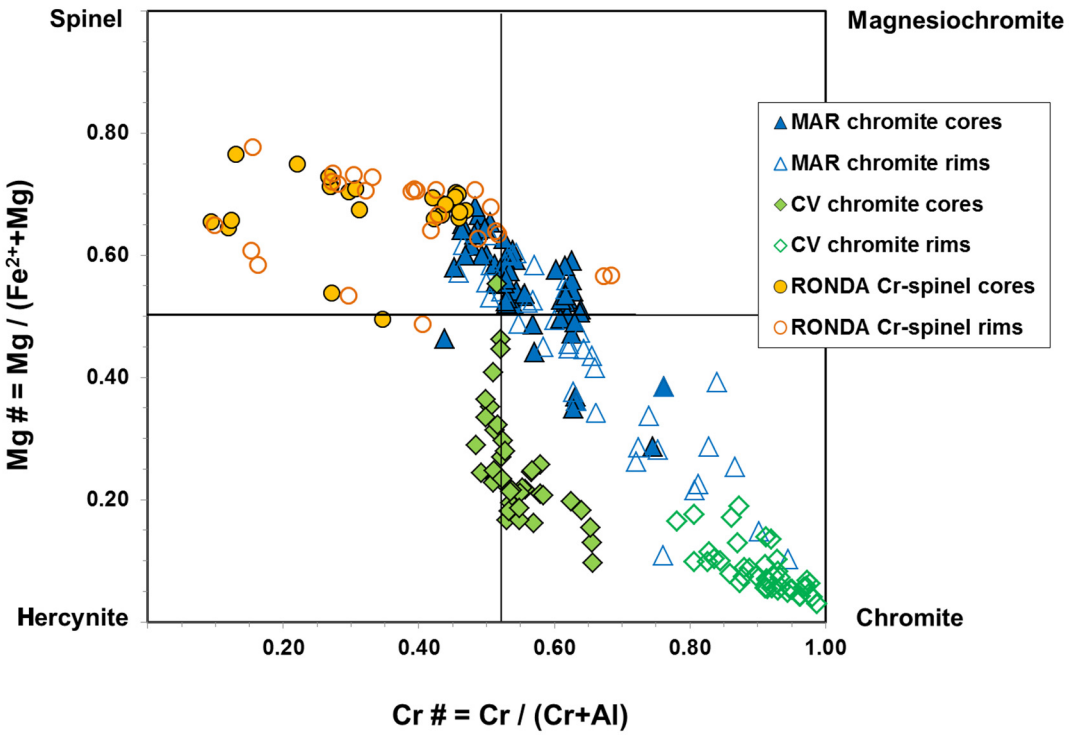

Figure 3. Mg# vs. Cr# plot of chromite cores and rims of the MAR, CV and Ronda samples.

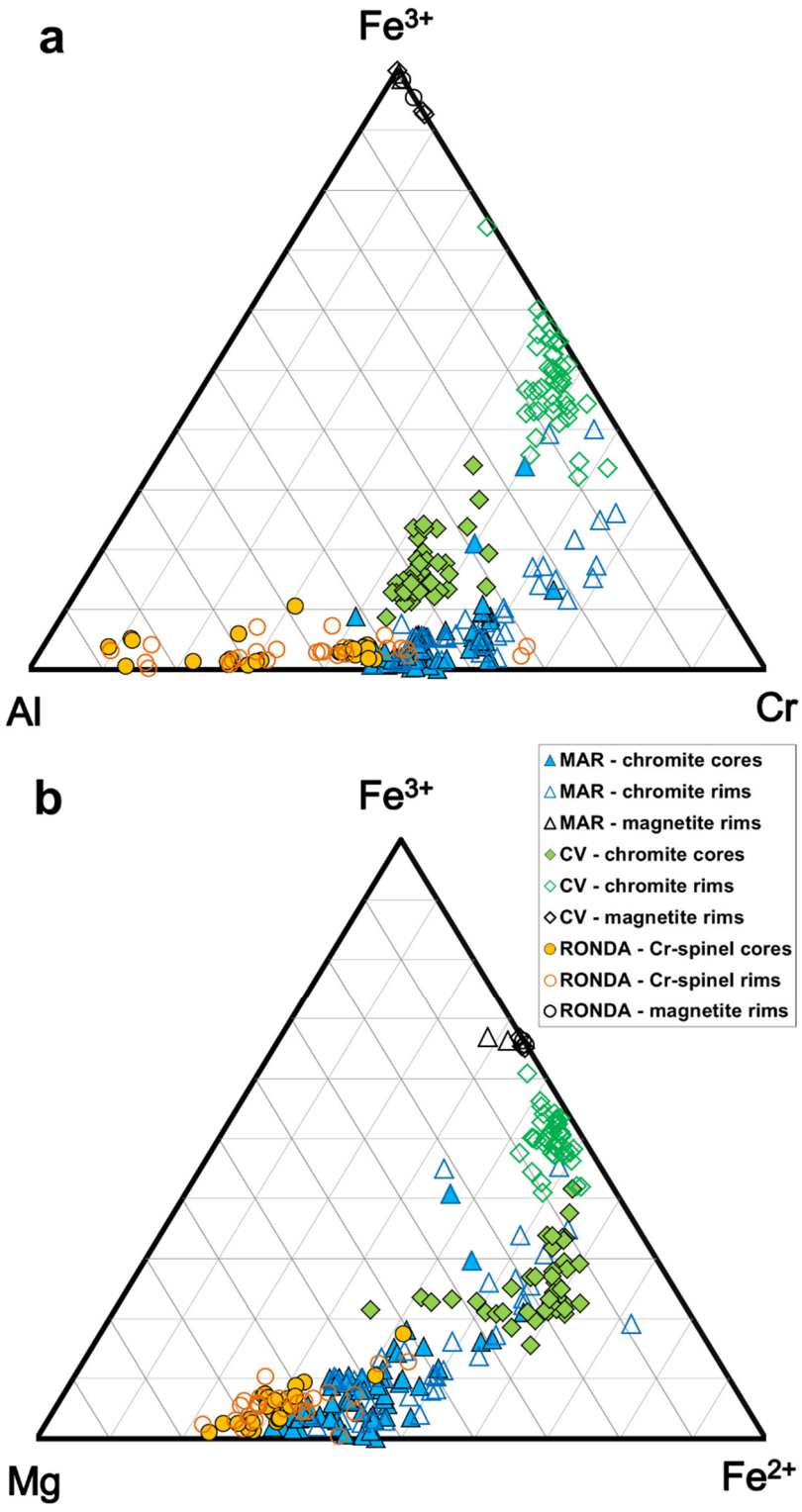

Figure 4. Ternary plots (**a**) Al-Cr-Fe^{3+} and (**b**) Mg-Fe^{2+}-Fe^{3+} for the cores and rims of the MAR magnesiochromites, CV chromites, and Ronda chromian spinels.

EMP data for MAR chromites (Tables A1 and S1; Figure 3) confirm petrographic observations: most non-opaque chromite cores are magnesiochromites, with Mg# = 0.68–0.29 and Cr# = 0.44–0.76, whereas corresponding chromite rims stray towards Fe- and Cr-richer compositions (Mg# = 0.63–0.10 and Cr# = 0.46–0.95). Opaque chromite grains, found in samples FL-02-03, FL-08-04, FL-08-11, FL-10-15, SAL-09-02A, SAL-09-06, and FL-DR-07-01,

invariably have ferritchromit compositions (Cr# = 0.53–0.95, Mg# = 0.61–0.10), indicating more advanced oxidation than has occurred in those rocks where ferritchromit only forms a thin rim around primary magnesiochromite. The composition of the ubiquitous primary magnesiochromite relics in the serpentinized harzburgites and dunites from the Rainbow and Saldanha sites [13,14,56] confirms the highly refractory character of the uppermost mantle underneath these MAR areas, as previously recognized [25,27,37,57].

Most relic CV grains have chromite cores, exhibiting Mg# = 0.55–0.10 and Cr# = 0.48–0.66, with rims straying towards true ferritchromit compositions, Mg# = 0.19–0.03 and Cr# = 0.78–0.99 (Figure 3; Tables A1 and S1).

The chromian spinels of the Ronda serpentinites have typical spinel cores (Mg# = 0.77–0.55 and Cr# = 0.09–0.47), and their rims show signs of more restricted oxidation than the other two sets, with Mg# = 0.78–0.49 and Cr# = 0.10–0.68 (Figure 3; Tables A1 and S1).

From the three populations, relic spinels from MAR serpentinites are the richest in Cr (>1 *apfu*), whereas those from Ronda serpentinites are the richest in Al (>>1 *apfu*).

Oxidation is incipient in both populations (mostly, $Fe^{3+}/(Fe^{2+}+Fe^{3+}) < 25\%$, and (Cr + Al) $\geq$ 1.75 *apfu*), but relic CV chromites are considerably more oxidized ($Fe^{3+}/(Fe^{2+} + Fe^{3+}) = 20–45\%$, and (Cr + Al) = 1.80–1.25 *apfu*). The #Cr/#Fe ratio is much higher in MAR relic magnesiochromites (mostly >1) than in CV chromites (mostly <1), whereas Ronda relic spinels spread over the whole range (~1.2–1.6; Tables A1 and S1).

Progressive loss of Al and Mg, and concomitant relative enrichment in Cr, Fe^{3+} and Fe^{2+}, during chromite oxidation, are evident in the composition of chromite rims and depicted in Figures 3 and 4, as well as on X-ray profiles (Figure 2). A few grains where oxidation has gone a step further exhibit an outer rim of magnetite (Table S1), indicating extensive loss of all other major chromite components, including Cr.

Although not all trace components were measured or detected in the three sampled populations, some comparisons could be made: minor components such as Mn, Ti and V are lowest in the Ronda spinels, whereas CV chromites tend to be richer in Ti, Mn, Zn, and for the most part also in Ni than the MAR magnesiochromites and Ronda chromian spinels (Tables A1 and S1); in the latter population, Zn, Ni and Co were not detected. The MAR and Ronda populations seem quite similar in their low trace component contents.

5. Discussion

5.1. Alteration Rims or Overgrowths?

On the basis of previous work [3], Ulmer (1974) [4] defended that ferritchromit rims surrounding chromite grains of the Pennsylvania-Maryland State Line serpentinites were secondary overgrowths on the original chromite, using several arguments to put aside the possibility that such rims might simply be an alteration product of the original chromite grains.

However, the petrographic evidence from the MAR, CV and Ronda serpentinites, and the well-known limited mobility of Cr, have made us take a different view: (i) in most grains of the studied samples, ferritchromit occurs not only as an enveloping rim of variable width, but also bordering the fractures that chromite grains often exhibit (Figure 2); (ii) besides chromite, the only other Cr-bearing mineral in the serpentinites protolith is orthopyroxene; given the restricted amount of orthopyroxene in the original harzburgites (usually <10 modal%, easily ascertained by the amount of bastite serpentine, i.e., the corresponding orthopyroxene-pseudomorphs, where primary pyroxene has been replaced) and the limited mobility of Cr (most of which remains in bastite serpentine; [15]), it would be quite unlikely that all chromite grains disseminated throughout the serpentinized rock would exhibit ferritchromit overgrowths.

Moreover, and also in contradiction with Ulmer's observations [4], the occasional Cr-rich chlorite found in the studied serpentinites is spatially quite close to the chromite grains [15].

Therefore, it seems likeliest that the ubiquitous ferritchromit (±magnetite) rims of the chromite grains from the MAR, CV and Ronda serpentinites are indeed oxidation rims, resulting from the extremely slow diffusion of Mg and Al out of the original chromite grains (with consequent relative enrichment of Fe and Cr), during serpentinization of the host ultramafic rocks. This is also the interpretation of several other authors (e.g., [8–11]), for similar occurrences.

Incomplete magnetite rims are rare in the studied chromite populations, and are probably due to very localized and extreme conditions (such as higher fluid/rock ratios, more oxidizing fluids, and/or more prolonged fluid-rock interaction) which have enabled Cr leaching and (proximal) diffusion out of the chromite borders.

5.2. Chromite Oxidation Patterns

Chromite oxidation associated to serpentinization of the host peridotites has been extensively studied in great detail (e.g., [3–11]), and the three study cases presented here closely conform to the general patterns described by those authors. As shown in Figure 3, magnesiochromite, chromite and chromian spinel rims tend to ferritchromit compositions, displaying progressive increase in their Cr# and simultaneous decrease in their Mg#.

According to these and other authors, chromite oxidation includes two steps, namely, (*i*) chromite transition to ferritchromit, and (*ii*) ferritchromit transition to magnetite. The latter step implies extreme oxidation rates or very prolonged oxidation, and has been observed only in a few rims of the chromite grains in this study. The ternary Al-Cr-Fe^{3+} and Mg–Fe^{2+}-Fe^{3+} plots of Figure 4 show that the three sample sets basically follow the same two-step compositional trend during oxidation: the first stage, characterized by progressive Mg and Al loss, produces increasingly ferritchromitic compositions; on the final stage, Cr is eventually mobilized and removed, and magnetite rims may form.

Tables A1 and S1 and Figure 4 also show that spinel oxidation, and eventual formation of ferritchromit rims, has been more intense in the CV serpentinites (on average ~20% increase in $Fe^{2+}/(Fe^{2+} + Fe^{3+})$, compared with what is observed in the MAR and Ronda serpentinites (average increases of ~10% and ~4%, respectively). Simultaneous Mg and Al depletion and relative increases in Cr# and Fe# follow the same trend (Tables A1 and S1; Figures 4 and 5): CV (aver. ΔMg ~−14%, ΔAl ~−29%, ΔCr# ~33%, ΔFe# ~15%)—MAR (aver. ΔMg ~−13%, ΔAl ~−11%, ΔCr# ~10%, ΔFe# ~14%)—Ronda (aver. ΔMg ~ −6%, ΔAl ~ −8%, ΔCr# ~8%, ΔFe# ~7%).

It is interesting to observe that, notwithstanding their very different settings and their different histories, these three chromite sets display very coherent oxidation patterns: both Mg# (Figure 5a) and Cr# (Figure 5b) of the three populations exhibit the same trend with increasing $Fe^{3+}/(Fe^{2+} + Fe^{3+})$ ratios towards the rims, the same happening with the variation trends of the (Cr + Al) and (Al + Mg) values, which decrease progressively with increasing oxidation rates (Figure 6a,b), indicating this process also involves a progressive loss of Al.

In contrast to the trends obtained for the variation of major chromite components with increasing $Fe^{3+}/(Fe^{2+} + Fe^{3+})$ ratios, the equivalent trends for trace elements (Figure 7) show that not all chromite populations have similar contents or behave in the same way. As said above, CV chromites are richer in Ti, Mn, Zn (±Ni, Co) than the MAR magnesiochromites and the Ronda chromian spinels, whereas these two populations are quite similar in their low trace component contents (Figure 7).

The slight enrichment observed for Mn during chromite oxidation (Figure 7a), is much less obvious for Ti and V (Figure 7d,e); no significant change in Ni or Co can be perceived (Figure 7c,f), and the strong Zn depletion is only observed in the CV population (Figure 7b).

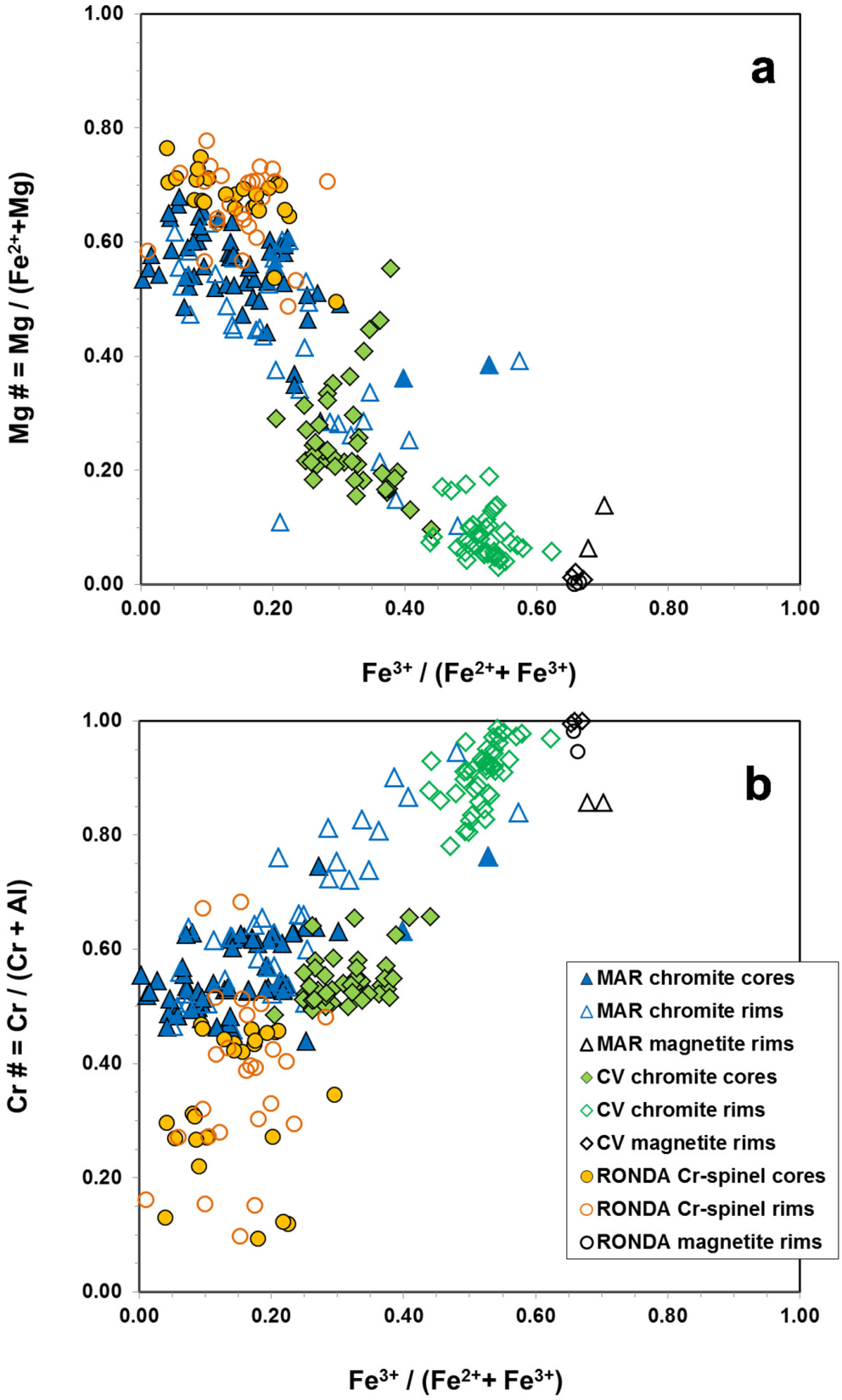

Figure 5. Oxidation trends of the MAR magnesiochromites, CV chromites and Ronda chromian spinels: (**a**) Mg# vs. $Fe^{3+}/(Fe^{2+} + Fe^{3+})$ and (**b**) Cr# vs. $Fe^{3+}/(Fe^{2+} + Fe^{3+})$.

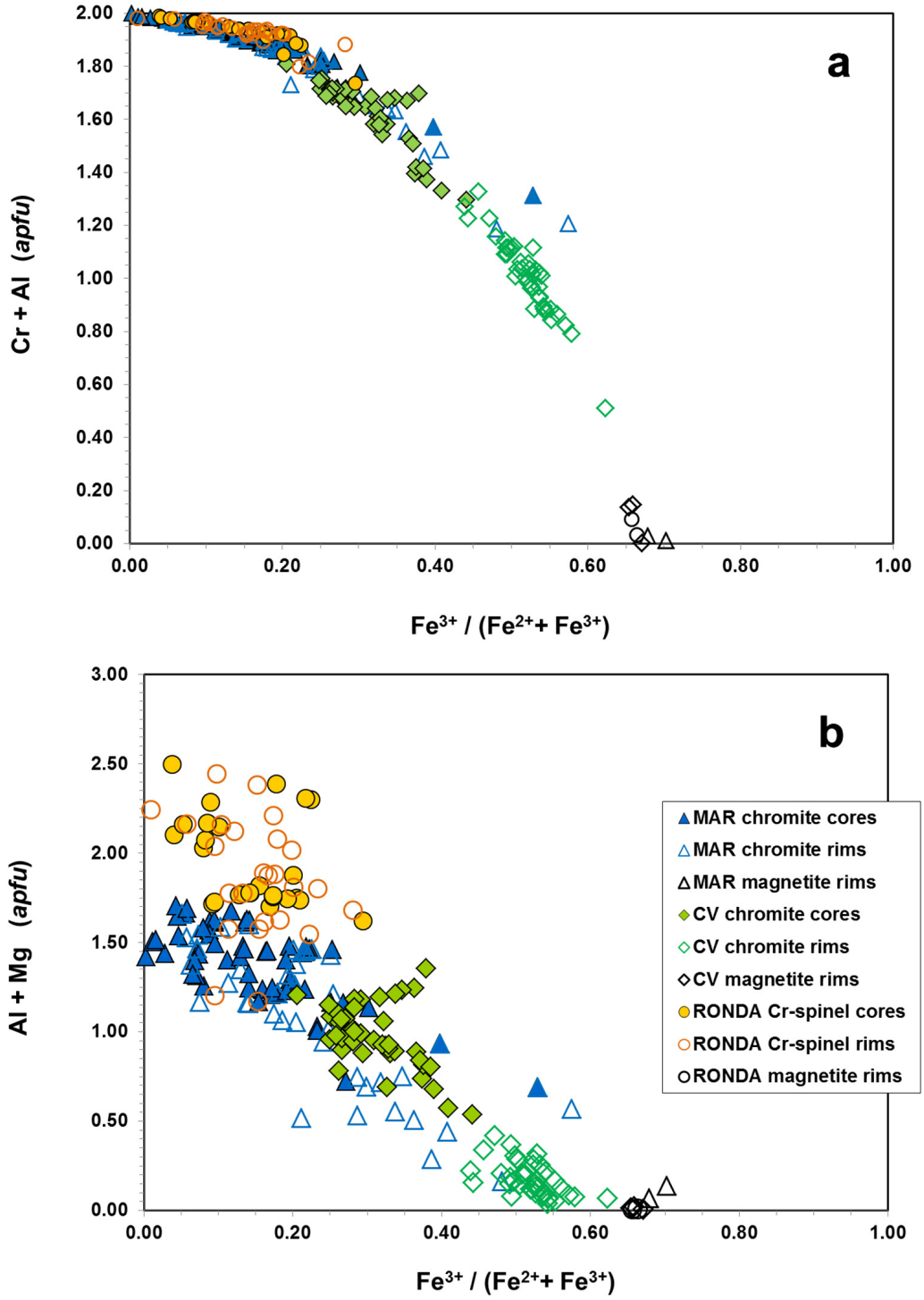

Figure 6. Oxidation trends of the MAR magnesiochromites, CV chromites, and Ronda chromian spinels: (**a**) (Cr + Al) vs. $Fe^{3+}/(Fe^{2+} + Fe^{3+})$ and (**b**) (Al + Mg) vs. $Fe^{3+}/(Fe^{2+} + Fe^{3+})$.

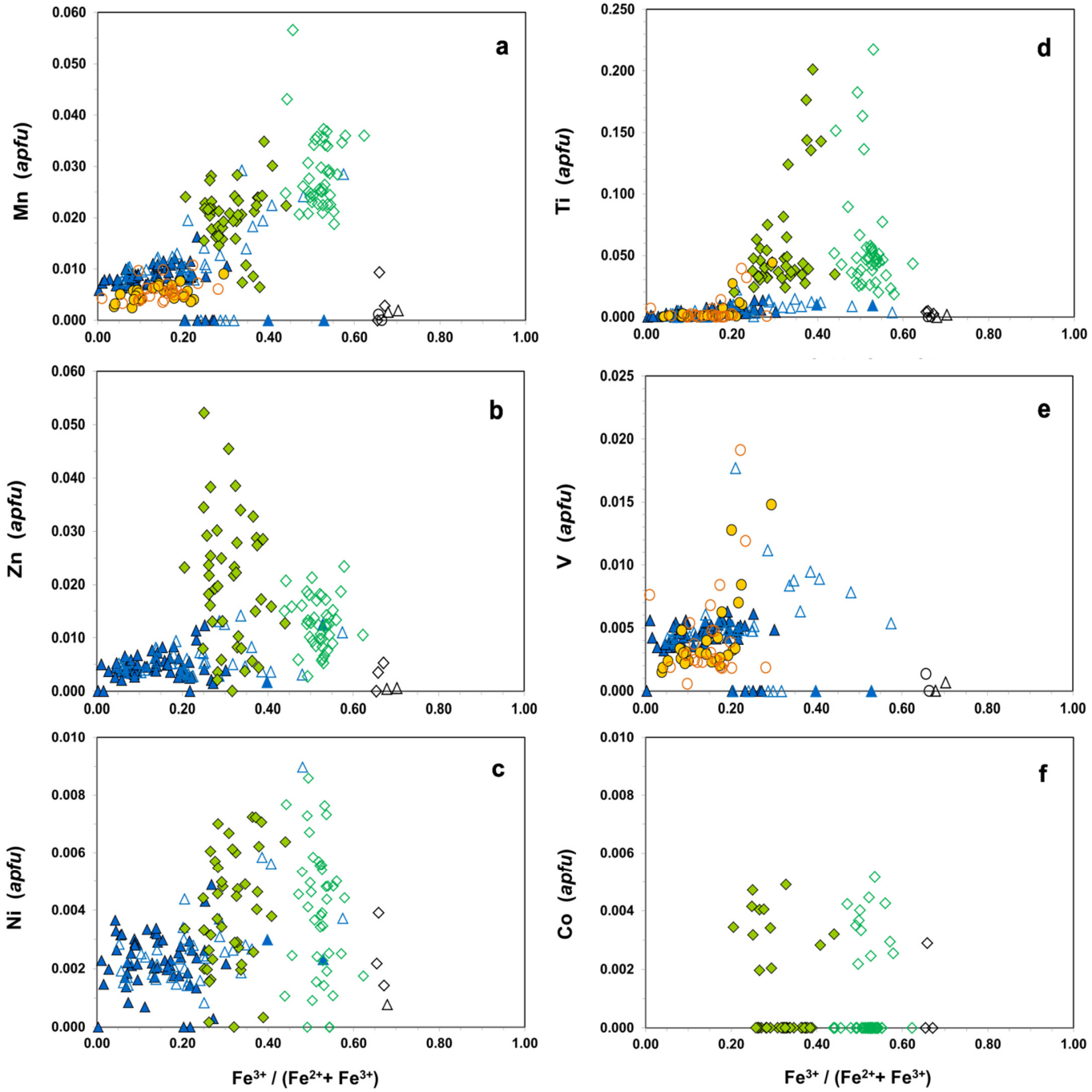

Figure 7. Trace element variation during oxidation of the MAR magnesiochromites, CV chromites, and Ronda chromian spinels: (**a**) Mn; (**b**) Zn; (**c**) Ni; (**d**) Ti; (**e**) V; (**f**) Co. Symbols as in Figure 6.

5.3. Relative Mobility of Components during Chromite Oxidation

Being impossible to retrace the events from which chromite oxidation resulted in the three serpentinite sets under study and to infer the specific conditions under which it took place, the best way to assess the relative mobility of chromite components during oxidation has been to evaluate major compositional changes (ΔX) against increasing Fe oxidation rates, $\Delta Fe^{3+}/(Fe^{2+} + Fe^{3+})$, in each chromite set (Figures 8 and 9).

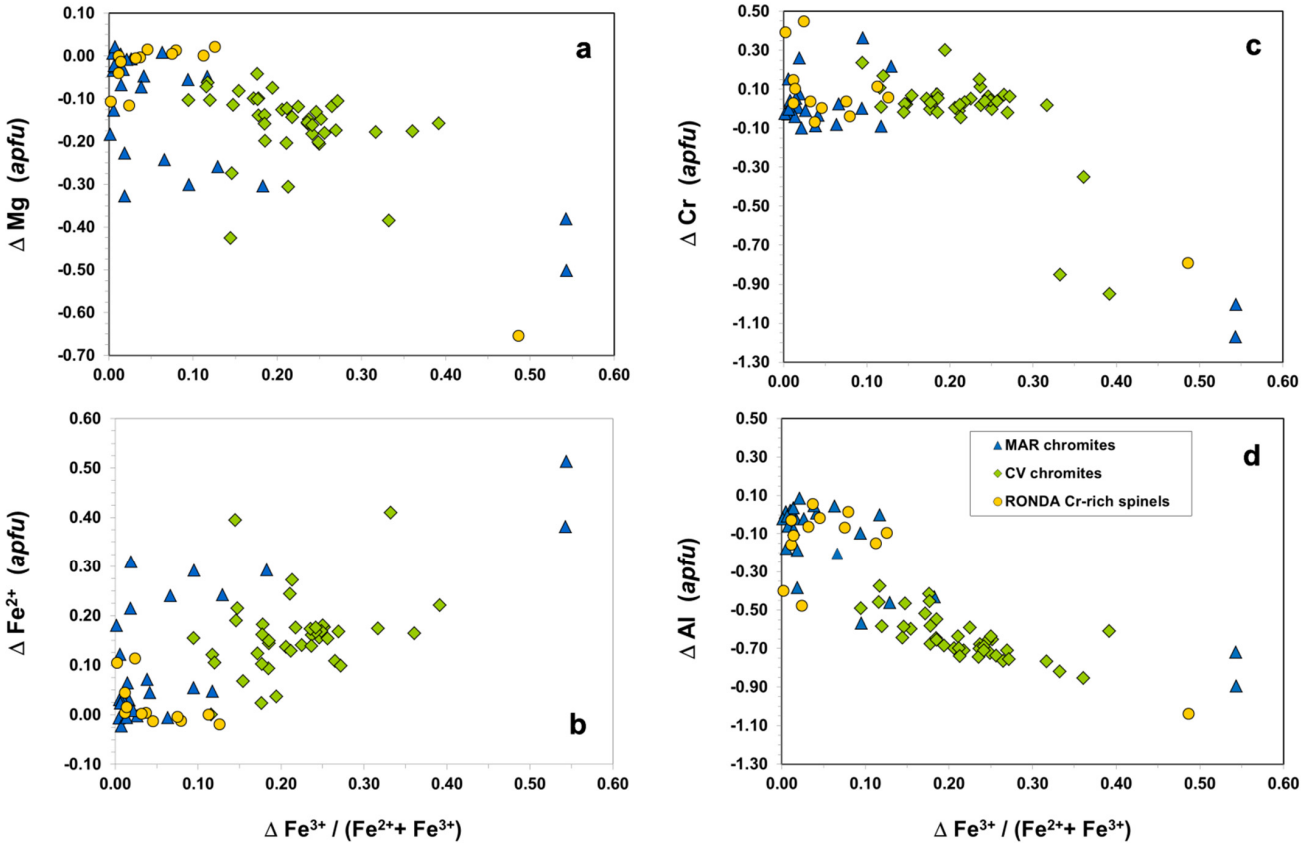

Figure 8. Variation of (**a**) Mg, (**b**) Fe^{2+}, (**c**) Cr and (**d**) Al contents with increasing Fe oxidation rates in the MAR magnesiochromites, CV chromites, and Ronda chromian spinels.

Considering the variation of each major component of chromite with the oxidation rate (Figure 8), it is apparent that: (*i*) the expected Mg-Fe^{2+} covariance in the A (tetrahedral) position controls the variation rates of these two metals, though the MAR and CV chromite sets show a general trend of decreasing Mg and increasing Fe^{2+} with increasing oxidation rates (Figure 8a,b); (*ii*) Cr concentration is fairly constant up to Fe oxidation rates of 30%, when it drops drastically with the onset of magnetite (Figure 8c), and (*iii*) there is a more consistent trend for Al, which decreases progressively with increasing oxidation rates (Figure 8d); this trend is particularly well-defined for the CV chromite set, probably because it covers a wider range of oxidation rates.

These preliminary inferences are further confirmed when the variation of several major component ratios are plotted against Fe oxidation rates in chromite (Figure 9): (*i*) as already implied by the diagrams of Figure 8a,b, the $Mg/(Fe^{2+} + Mg)$ ratio does not seem a very reliable parameter, as shown by the dispersion observed in Figure 9a, mainly due to the variable $Mg/(Fe^{2+} + Mg)$ ratios in the original chromite grains, even in the same set; (*ii*) taking into account the diagrams in Figure 8c,d and confronting the changes in the $Cr/(Cr + Al)$ and $Cr/(Cr + Al + Fe^{3+})$ ratios (Figure 9b,c), it becomes clear that the significant increase of the $Cr/(Cr + Al)$ ratio in the first stages of chromite oxidation (before the onset of magnetite) is misleading, and is due, not to an actual increase in Cr, but rather

to the substantial loss of Al, as the Fe^{3+}/Fe^{2+} proportion in chromite increases; this is further confirmed by the variation pattern for the $Al/(Cr + Al + Fe^{3+})$ ratio (Figure 9d), which shows a steady decrease with increasing chromite oxidation rates; (*iii*) the increasing loss of Al during oxidation of the CV chromites, even for oxidation rates lower than 30%, defines indeed good linear trends (Figures 8d and 9d–f), which even the MAR and Ronda sets seem to fit, notwithstanding the dispersion observed for these two sets at very low oxidation rates; (*iv*) when the increase in Fe oxidation rates exceeds ~30%, however, Cr contents drop drastically, marking the beginning of the second oxidation step whereby ferritchromit starts to give way to magnetite (Figures 8c and 9c,e); (*v*) indeed, and in spite of some dispersion observed at very low oxidation rates (<10%), loss of Mg + Al defines a consistent downward curve (Figure 9f) and seems a dominant feature during the first stages of chromite oxidation, and tends to increase steadily with increasing $Fe^{3+}/(Fe^{2+} + Fe^{3+})$ rates, especially when they exceed 15%–20%.

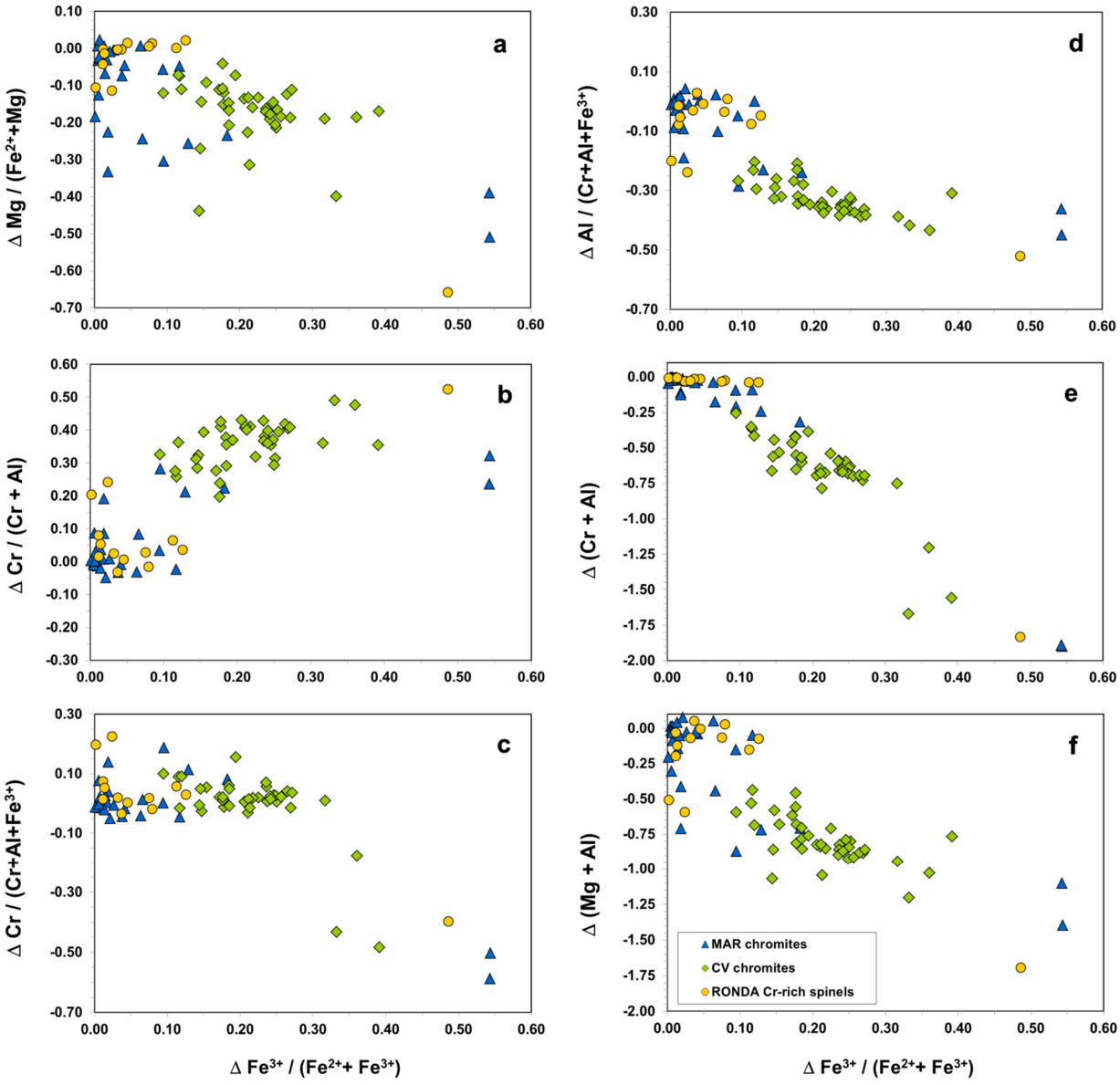

Figure 9. Variation of (**a**) $Mg/(Fe^{2+} + Mg)$, (**b**) $Cr/(Cr + Al)$, (**c**) $Cr/(Cr + Al + Fe^{3+})$, (**d**) $Al/(Cr + Al + Fe^{3+})$, (**e**) (Cr + Al) and (**f**) (Mg + Al) with increasing Fe oxidation rates in the MAR magnesiochromite, CV chromites and Ronda chromian spinels.

Of the three chromite populations under study, the CV set seems to define the most complete and consistent trends, whereas the MAR and Ronda sets show wider dispersion. This may be due, at least in part, to the narrower $\Delta Fe^{3+}/(Fe^{2+} + Fe^{3+})$ range in the latter two sets, and also to the fact that CV serpentinites are the oldest, so that chromite oxidation may have lasted longer and been more thorough than in the other settings. Although fewer MAR and Ronda samples attain very high oxidation rates, they also seem to follow the same trend, with dramatic loss of Cr as $Fe^{3+}/(Fe^{2+} + Fe^{3+})$ ratios increase and exceed 50% (Figure 9c,e).

The variation patterns obtained against increasing Fe oxidation rates are confirmed when plotted against increasing Cr/(Cr + Al) ratios (Figures 10 and 11): with increasing Cr/(Cr + Al) ratios, as the chromite–ferritchromit transition proceeds, the rate of Mg loss in the MAR chromites is higher than in either the CV chromites or the Ronda Cr-spinels (Figures 10a and 11a), whereas Al loss in the three chromite sets defines a perfect linear trend (Figures 10c and 11c). This might just be due to the fact that MAR magnesiochromites are richer in Mg than CV chromites and have probably undergone more intense oxidation than Mg-richer Ronda chromian spinels, or else would mean that some specific condition(s) may control Mg loss during the first stage of chromite oxidation, producing different trends for the MAR and CV (and Ronda) chromite sets, whereas Al loss is steadier.

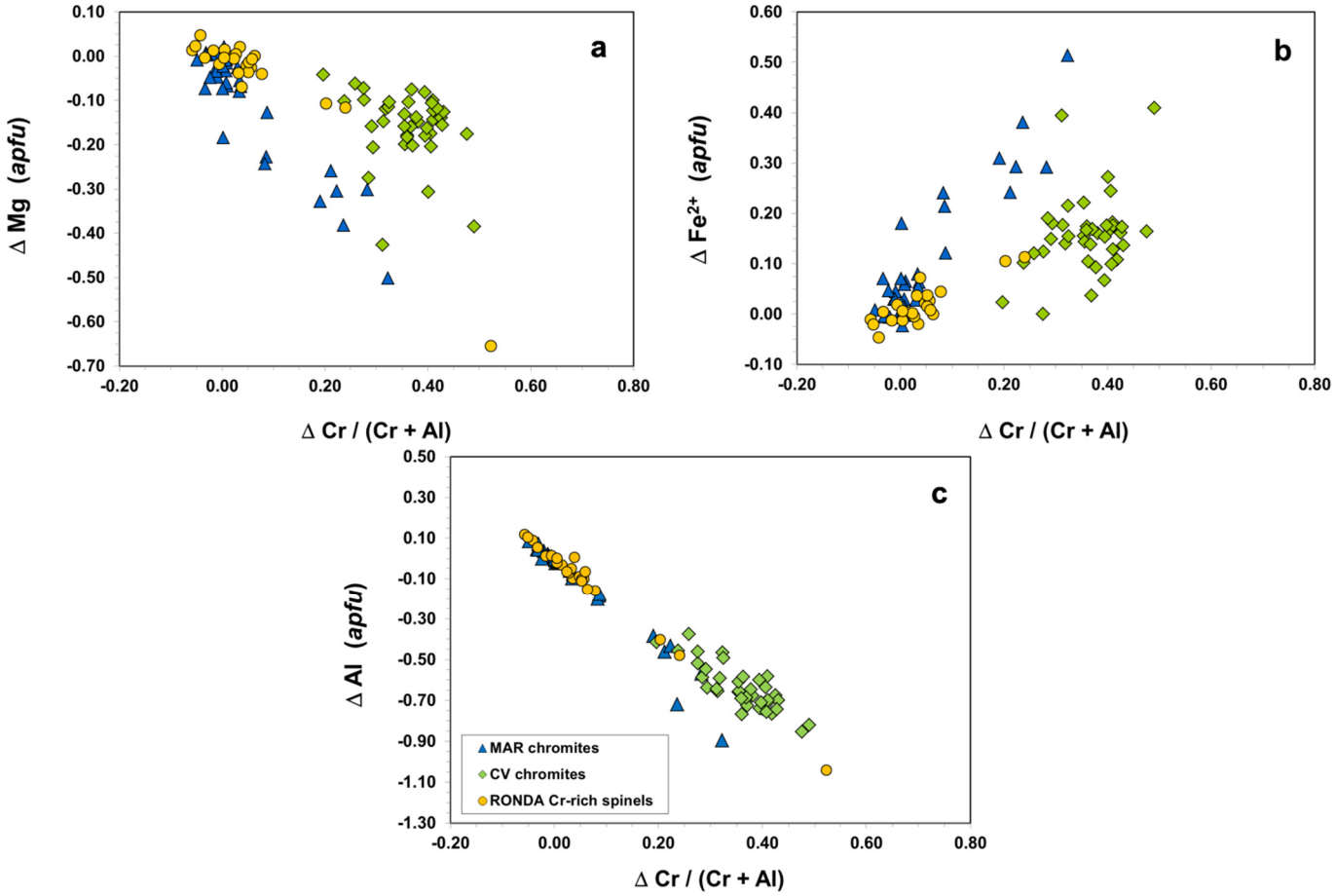

Figure 10. Variation of (**a**) Mg, (**b**) Fe^{2+} and (**c**) Al contents with increasing Cr/(Cr + Al) ratios in the MAR magnesiochromites, CV chromites and Ronda chromian spinels.

On the other hand, it is also worth noting that, in absolute terms, Al loss is much more dramatic in the CV chromites (Figures 8d, 9d and 10c) than in the other two sets, implying very specific, Al mobility-enhancing conditions during serpentinization. Indeed, considering that Al and Mg losses are probably simultaneous along the oxidation process,

they would be expected to follow the 2:1 stoichiometric proportions of the two elements in the spinel structure, as Fe^{2+} is oxidized to Fe^{3+}, for reasons of electrostatic balance. This is approximately what is seen for the MAR and Ronda sets, but not for the CV chromites, which show Al depletion in a proportion higher than 2:1 relative to Mg loss, at most oxidation rates (Figure 8d). It would seem, then, that some different fluid feature(s) might have been responsible for this enhanced Al loss during oxidation of the CV chromites. However, it must be remembered that CV chromites have the lowest Mg contents and those are practically removed in the ferritchromit rims (Mg < 0.1 *a.p.f.u.* in most analysed rims), with the exception of those grains from deeper-seated serpentinites (depth > 85 m); this means that, after losing their Mg, they will continue to lose Al to accommodate more Fe^{3+} in the B position, as oxidation proceeds.

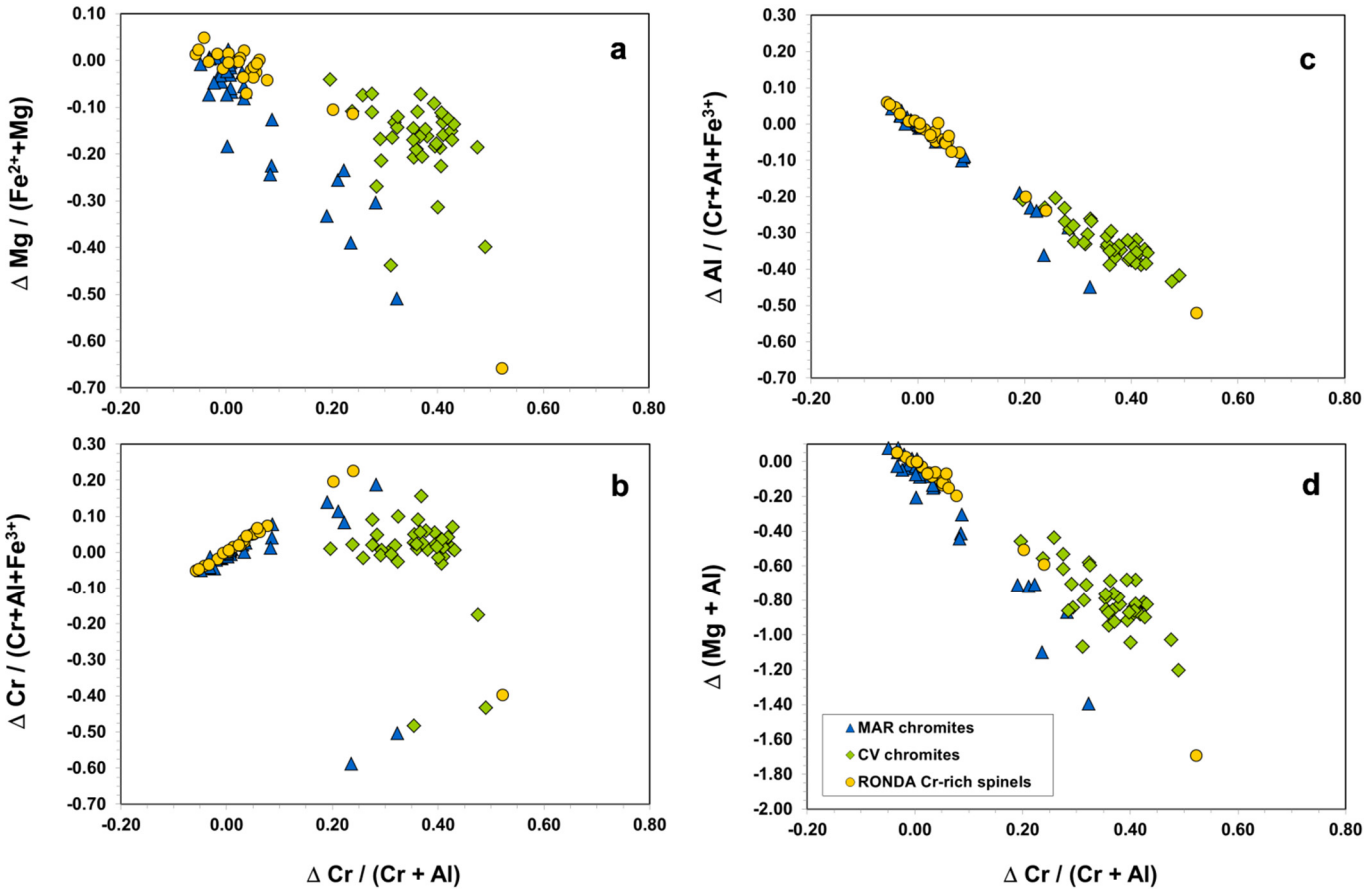

Figure 11. Variation of (**a**) Mg/(Fe^{2+} + Mg), (**b**) Cr/(Cr + Al + Fe^{3+}), (**c**) Al/(Cr + Al + Fe^{3+}) and (**d**) (Mg + Al) with increasing Cr/(Cr + Al) ratios in the MAR magnesiochromites, CV chromites and Ronda chromian spinels.

The progressive loss of Al, and eventually Cr, which occurs during chromite oxidation in peridotites undergoing serpentinization, clearly shows that these two elements may not be always "immobile" during hydrothermal alteration as often assumed [58].

The variation trends of the analysed trace elements (Mn, Ti, V, Ni, Co and Zn) during chromite oxidation are more difficult to evaluate, given their low concentration and associated analytical error. At first glance, these elements seem to be relatively immobile during chromite oxidation and may become slightly enriched in the ferritchromit rims (Figures 7 and 12), though some depletion may occur in part of the CV chromite population (Figure 12).

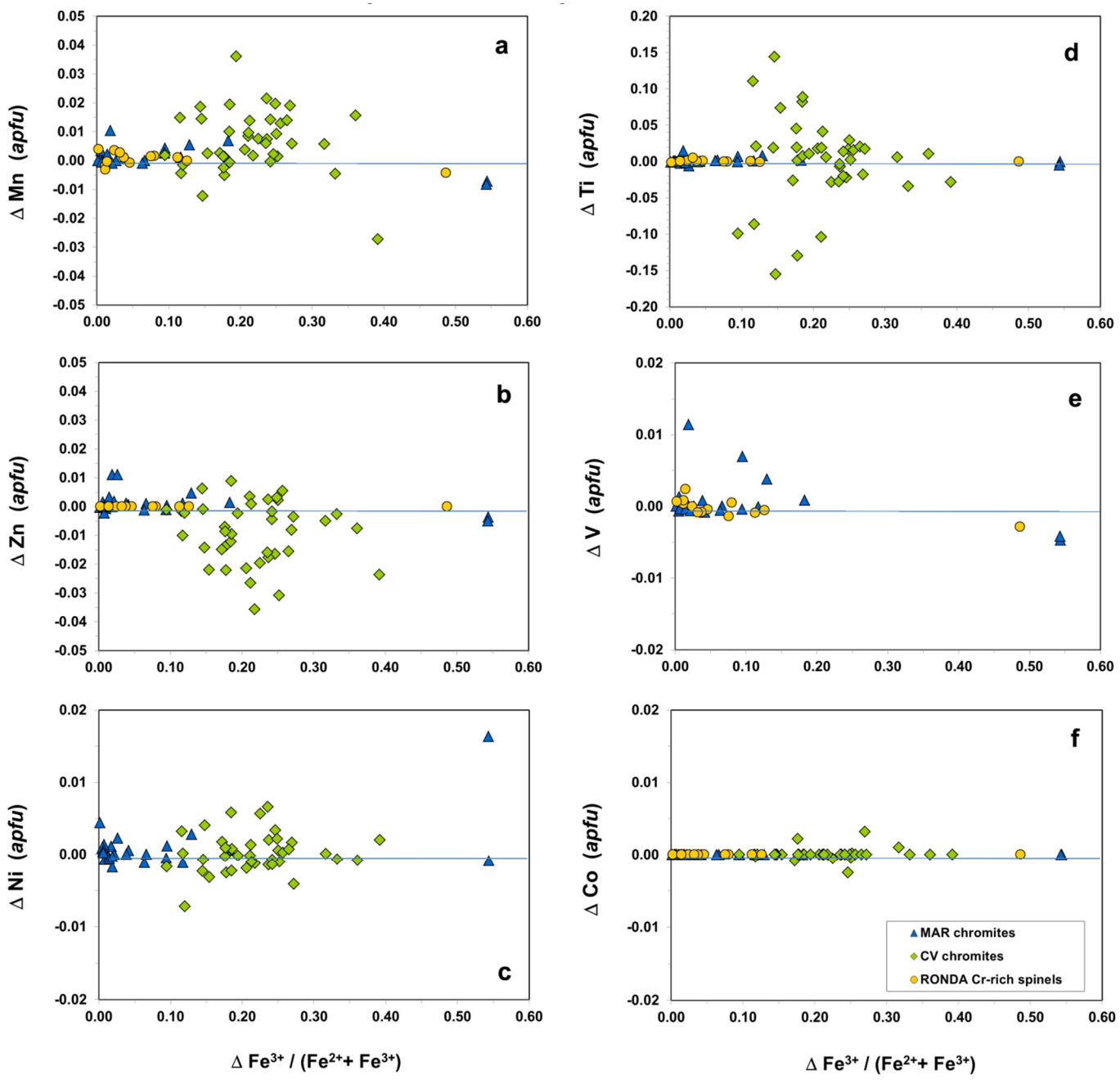

Figure 12. Variation of trace components (**a**) Ti, (**b**) V, (**c**) Mn, (**d**) Ni, (**e**) Zn and (**f**) Co with increasing Fe oxidation rates in the MAR magnesiochromites, CV chromites and Ronda chromian spinels.

Nonetheless, some interesting inferences can be gathered when plotting trace element variation against the variation of chromite oxidation rates (Figure 12): it is immediately evident that V and Co contents in the three studied sets exhibit no major change with increasing chromite oxidation rates (Figure 12e,f); for the other trace elements (Ti, Mn, Ni and Zn), only the CV chromites show significant change with increasing chromite oxidation rates (Figure 12a–d) and not always in the same direction. Indeed, only Mn and Zn in the CV chromites produce relatively consistent variation trends, an essentially positive trend in the case of Mn (Figure 12a) and a depletion trend for Zn (Figure 12b), whereas neither Ti nor Ni variation patterns seem to correlate very well with increasing oxidation rates (Figure 12c,d).

The variation patterns of the same trace elements during the chromite–ferritchromit transition, i.e., as the Cr/(Cr + Al) ratio increases, are very similar to those obtained against increasing $Fe^{3+}/(Fe^{2+} + Fe^{3+})$ rates, showing very little or no trace element variation in the MAR and Ronda sets (Figure 13), whereas the CV chromites display significant gain and depletion patterns for Mn and Zn, respectively (Figure 13a,b), mixed variation patterns for Ti and Ni (Figure 13c,d) and almost no variation in their V and Co contents (Figure 13e,f).

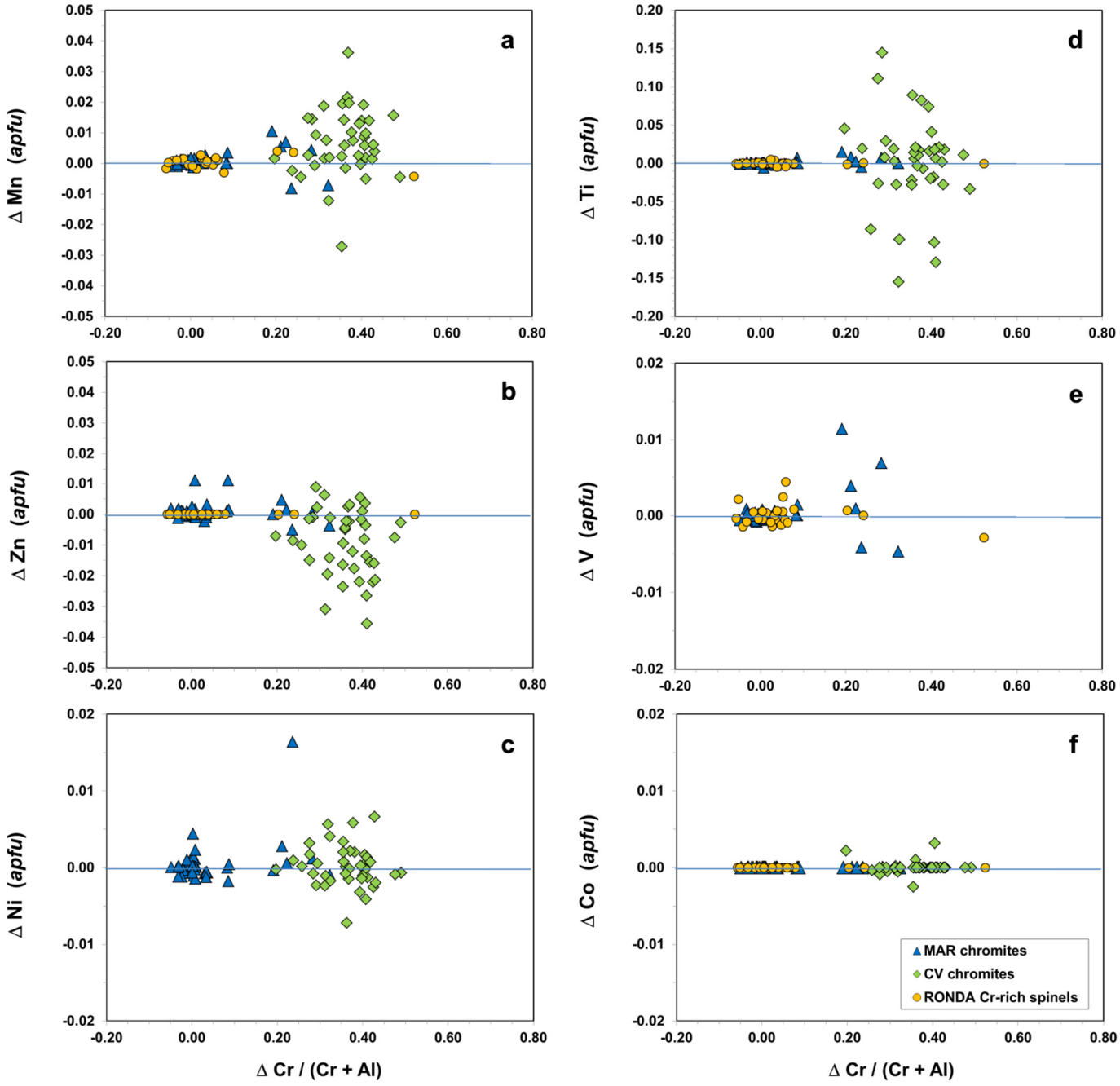

Figure 13. Variation of trace components (**a**) Ti, (**b**) V, (**c**) Mn, (**d**) Ni, (**e**) Zn and (**f**) Co with increasing Cr/(Cr + Al) ratios in the MAR magnesiochromites, CV chromites and Ronda chromian spinels.

Of the six trace elements considered in this study, only V and Co might therefore be considered immobile during the chromite oxidation process, and none defines a linear variation trend that could be used to investigate possible distinctions among the three chromite populations along the oxidation process. According to the variation depicted in the diagrams of Figure 7, Zn seems to be the most mobile trace element during chromite oxidation, though this trend is most obvious in the CV chromites, probably because they have been subject to the oxidation process for a longer extent than the other two populations. Given their negatively correlating patterns, Zn depletion may be the cause of the relative Mn enrichment observed in the CV chromite rims (Figure 12a,b).

One thing, however, is common to all three chromite sets: with the exception of Ni (Figure 7c), all trace elements in chromite and ferritchromit are leached in the final oxidation event responsible for the formation of magnetite rims (Figure 7a,b,d–f), implying very drastic conditions, namely those concerning water/rock ratios and pH of the serpentinization fluid. In a tentative parallel between the behaviour of these trace elements in an oxide and in aqueous Cl^- or F^- complexes (data from [59]), it might be said that indeed Ni would show the lowest mobility, being much less soluble than the other elements, whereas Zn would be the most mobile, therefore explaining its drastic depletion in the CV ferritchromit rims, where serpentinization-related fluids have been at work for a considerably longer span of time.

5.4. The Role of Fluid Composition and Fluid/Rock Ratios in Chromite Oxidation

Temperature and water/rock ratios, the main factors controlling the extent of serpentinization and serpentine evolution (e.g., [15,60–62]), are parameters not easy to estimate or infer, and may not be the most prominent factors in chromite oxidation.

Oxygen-isotope-based serpentinization temperatures in the order of 350–200 °C and approximate water/rock ratios ranging from 0.6 to 4.5 were estimated for the MAR serpentinized harzburgites [13,15]. Such values, well above the minimum values for serpentinization to proceed [62–64], greatly favour the oxidizing conditions responsible for the high $Fe_2O_3/(FeO + Fe_2O_3)$ ratios in the MAR serpentinites (0.65–0.91; [15]) and for the ubiquitous oxidation of magnesiochromite rims to ferritchromit.

Although the estimated volume increase during serpentinization of MAR peridotites (26%–27%; [15]) and CV peridotites (28%–31%; Ribeiro da Costa, *unpubl. data*) are quite close, no temperature or water/rock ratio estimates for CV and Ronda serpentinites are available yet, making it harder to compare chromite oxidation patterns in the studied sets on the basis of these two factors.

Petrographic evidence has shown that the progress of chromite oxidation does not seem to follow serpentine evolution very closely: chromite grains in mesh serpentinites are as likely to show ferritchromit rims, or even ferritchromit cores, as those in texturally more evolved serpentinites, and Fe oxidation rates are not necessarily always higher in serpentinites exhibiting more evolved, recrystallized and non-pseudomorphic textures [13,15]. Indeed, the fact that pseudomorphic serpentine textures predominate in the CV serpentinites, as compared to the high proportion of non-pseudomorphic textures in MAR serpentinites, might imply lower water/rock ratios during serpentinization in the CV setting, and therefore limited rates and extent of chromite oxidation, which is in clear contradiction with the observation that CV chromites exhibit more extensive Fe oxidation and Al loss than the other two studied sets (Figures 4b, 5a, 8d, 9d and 10c). These observations suggest that other factors ultimately control the oxidation rates of chromite and the mobility of its components, namely the composition and pH of the intervening fluid and the extent of fluid-rock interaction.

Indeed, some experimental studies (e.g., [65]) have shown that variations in fluid acidity exert a much greater influence on the solubility of the majority of minerals than changes in temperature and pressure.

5.4.1. The Sepentinization Fluid

Assuming, then, that fluid composition is one of the main factors in chromite oxidation, it seemed fundamental to compare the serpentinization-related fluids in the three settings under study.

The geochemical (i.e., Br, B and U contents), $\delta^{18}O_{SMOW}$ and $^{87}Sr/^{86}Sr$ signatures of the MAR serpentinites indicate that unmodified seawater has been the fluid responsible for serpentinization [13,15]. Seawater is slightly alkaline in character (average pH = 7.8), and the small amount of magnetite in the MAR serpentinites implies that serpentinization-related protonation reactions (producing H^+ ions as the Fe-endmember of olivine is converted to magnetite) have been restricted and unlikely to cause significant pH changes in seawater during serpentinization.

The springwaters in the Cabeço de Vide area are structurally controlled and constitute a major hydrochemical province. Waters issuing from the Cambrian carbonates close to the Alter do Chão serpentinites are hypothermal, hyposaline, high Cl^--OH^--SO_4^{2-}-Na^+ waters, with very high pH values (11.5–12.0); waters issuing from the CV serpentinites, on the other hand, are only moderately alkaline (pH = 7.5–9.0) Mg^{2+}-HCO_3^- waters [66,67]. Similar bimodal hydrochemistry has been found in ultramafic-related waters from California and Oregon [68]: the moderately alkaline Mg^{2+}-HCO_3^-springs were interpreted as associated with surficial features and representing the discharge of shallow groundwater of meteoric origin; high Mg^{2+} concentrations would reflect the weathering of Mg-bearing minerals, such as serpentine (in soils, probably); the highly alkaline, Ca^{2+}-OH^- waters have only been found in areas underlain by fresh or partly serpentinized peridotites, probably emerging from a deep source (though non-magmatic and non-metamorphic), along faults or shear zones.

The Ronda serpentinized peridotites display variable, but usually low, contents in B and other volatiles. Studies carried out on these serpentinites [51] and on the intrusive leucogranites (e.g., [69]) have shown that (granite-derived) B-enriched fluids have been responsible for serpentinization, and that the Ronda peridotites have never been directly exposed to seawater. Spring-waters related to the Ronda peridotite can be classified into hyperalkaline fluids and river waters that are, respectively, similar to the Ca-OH and Mg-HCO_3 water types described in ophiolite-hosted alkaline springs elsewhere [54], as well as to those described for Cabeço de Vide [65,66]. The Ca-OH hyperalkaline fluids are characterized by relatively high pH (10.9–12), low Mg and high Na, K, Ca, and Cl^- concentrations and occur in the discharge sites and in natural ponds along the flow path of discharging fluids; as in other serpentinite-hosted (sub-) surface waters, the Ronda Mg-HCO_3 river waters are mildly alkaline (8.5 < pH < 8.9) and most likely due to hydrolysis of ferromagnesian peridotite minerals by infiltrated meteoric waters and shallow groundwater that are in equilibrium with the atmosphere. The physicochemical composition of Ronda Ca-OH hyperalkaline fluids is/was derived via low-temperature serpentinization reactions from Mg-CO_3 river waters or Ca-HCO_3 waters from near karst aquifers that infiltrate the peridotites along brittle faults with brecciated serpentinite [69].

These data indicate that the fluids responsible for serpentinization and consequent chromite and Cr-spinel oxidation in the studied settings were mildly alkaline (MAR) to hyperalkaline (CV and Ronda) in composition, thus favouring the solubility of aluminous minerals such as spinels (e.g., [64]) and, in particular, the mobility of Al, which may be greatly enhanced in fluids with pH > 6.5 (e.g., [65,70,71]).

Indeed, the experimental studies of Azimov and Bushmin on mineral solubility and element mobility [65] showed that: (*i*) the solubility of spinels and other Al-Fe minerals may increase by 1.0–4.5 orders of magnitude in alkaline solutions; (*ii*) at a pressure of 1 kbar, the solubility of aluminous minerals such as spinel decreases by 0.5–1.0 orders of magnitude with increasing temperature, both in acidic and alkaline solutions; (*iii*) the temperature dependence of solubility becomes weaker in very acidic and alkaline fluids, though the temperature effect on the solubility of spinellids remains negative and de-

creases with increasing pressure; and (*iv*) the solubility of these minerals increases with increasing pressure.

Furthermore, the mobility sequence for elements in alkaline solutions, established by Zaraiskii [70] at 500 °C, and confirmed by Azimov and Bushmin [65], indicates higher mobility for Al than for Mg and Fe (or Ti), whereas Al is known to be practically immobile in neutral solutions. Indeed, Azimov and Bushmin [64] refer that the mobility of Al increases markedly with increasing alkalinity, which would explain the extent of Al loss in the CV chromite rims during chromite oxidation (Figure 8d, Figure 9d,e, Figures 10c and 11c), in spite of the relatively low inferred water/rock ratios.

These experimental results mean that, even in low water/rock ratio contexts such as are suggested for Cabeço de Vide (and probably Ronda), highly alkaline serpentinization-related fluids may enhance both Fe oxidation and Al loss in chromite. Nevertheless, given the relative age of the three serpentinite sets, it seems likely that time, that is, the extent of water-rock interaction, may also be a decisive factor controlling these processes, explaining why the CV chromite set, of earlier age, exhibits the highest oxidation rates and Al depletion.

On the other hand, Fe oxidation and Al (±Zn) loss in Ronda chromian spinels are usually rather more restricted (<15% and <25%, respectively), when compared to the equivalent values in the MAR magnesiochromites (up to ~55% and ~45%) and CV chromites (up to 40% and 45%). This might be due to a conjunction of circumstances, namely the fact that serpentinization in Ronda is more recent than in Cabeço de Vide and, arguably, that it also happened under lower water/rock ratios than those estimated for the MAR serpentinites, as implied by the fact that Ronda samples are pseudomorphic serpentinites, some of them still containing a reasonable amount of relic olivine and pyroxene.

5.4.2. Rates and Extent of Serpentinization

Following multiple observations and experimental evidence (e.g., [72–74]) that serpentinization is greatly enhanced by hydrofracturing, it is quite likely that pervasive faulting in the studied MAR, CV and Ronda locations may have promoted and accelerated serpentinization.

Limited chromite oxidation rates in most MAR serpentinites ($\Delta\ Fe^{3+}/(Fe^{2+} + Fe^{3+}) <$ 20%; Figure 8) and unequilibrated $^{87}Sr/^{86}Sr$ signatures of some of these rocks [13,15] are evidence that serpentinization proceeded at relatively high speed, thus inhibiting extensive chromite oxidation and massive loss of chromite components, except for Mg (±Al).

On the other hand, the relative age of the peridotites undergoing serpentinization may also be an important factor in determining the extent of chromite oxidation: the CV chromites, hosted by the oldest (probably Ordovician) peridotites, display the strongest and more extensive alteration effects (highest Fe oxidation and Al ± Zn loss), compared to the MAR magnesiochromites (<1 Ma old) and Ronda chromian spinels (of Alpine age), probably due to their more prolonged interaction with serpentinizing fluids, in a tectonic setting that underwent regional metamorphism.

The fact that oxidation effects are less marked in the Ronda chromian spinels than in the other two sets may be due, either to their own original (more aluminous) composition and/or to the fact that serpentinization has been rather less extensive in the studied Ronda peridotites than in the other two serpentinite sets.

5.5. Chromite Oxidation Patterns as Footprints of Metasomatic and Metallogenetic Processes

The importance of chromite composition as a petrogenetic indicator in the study of mantle processes is well known.

If, as has been discussed in the present study, chromite oxidation patterns depend, at least, on such factors as water/rock ratios and fluid composition, the detailed analysis of those patterns may well have some relevance in studies focused on the serpentinization process undergone by ultramafic rocks, but also in metallogenetic studies concerning ores related to chromite-bearing ultramafic host-rocks. Such oxidation patterns are, therefore, very helpful to infer the history of the chromite-bearing rocks.

Even though chromite from the Nemeiben Ultramafic Complex, in Saskatchewan (Canada) may be almost unaffected during high-temperature partial serpentinization of the host peridotites [75], most chromites or chromian spinels do oxidize during serpentinization of their host-rocks (e.g., [3–15]), though variably so, according to the extent and conditions of serpentinization.

Furthermore, in the context of mafic-ultramafic-hosted massive sulphide deposits, such as occur in the South Urals (Russia), the extent of chromite alteration and the development of ferritchromit and magnetite rims have been ascribed to reactions with silicate minerals and hydrothermal fluids during early oceanic alteration, or subsequent hydrothermal circulation and sulphide deposition [76]. Similarly, important changes in the composition of chromites from sulphide-bearing samples have been reported in the Jinchuan Ni-Cu sulphide deposit (PRC) [77].

All these instances imply that chromite composition is sensitive to certain hydrothermal environments, and that detailed study of chromite alteration patterns may be a useful guide to a more comprehensive understanding of the physico-chemical conditions in the specific environment where ore-bearing mafic-ultramafic rocks occur.

6. Conclusions

As described by several authors in other geological and geotectonic settings, and irrespective of their original compositions, oxidation of magnesiochromite, chromite and chromian spinel in serpentinized peridotites from the Mid-Atlantic Ridge, the Alter do Chão pluton (Portugal) and the Ronda massif (Spain), respectively, produces ferritchromit (and, eventually, magnetite), following the same general pattern of Mg and Al depletion, and relative Fe and Cr enrichment. The data presented in this paper shows that Mg + Al depletion is relatively limited in the first stages of chromite oxidation (for $Fe^{3+}/(Fe^{2+} + Fe^{3+}) < 10\%–15\%$), becoming rather more severe for higher oxidation ratios. Cr mobility and depletion becomes apparent for $Fe^{3+}/(Fe^{2+} + Fe^{3+}) > 30\%$, and eventually ferritchromit may give way to magnetite.

Although a clear variation pattern is more difficult to obtain for trace components in the studied chromite sets, probably due to their low concentrations, most trace elements seem to be relatively immobile (especially Ni, Co and V), except for Zn, which undergoes marked depletion under high oxidation rates, and Mn, which may exhibit some relative enrichment.

Temperature and fluid/rock ratios being considered the most important factors controlling serpentinization, it would seem reasonable to assume they might also control spinel oxidation rates, and therefore also the depletion rates of spinel components. Nevertheless, the results obtained in the present study imply that oxidation trends are not closely controlled by temperature, but are, instead, conditioned by fluid/rock ratios, fluid chemistry (pH), and the extent of fluid-chromite interaction. Indeed, notwithstanding likely differences in the water/rock ratios and fluid compositions, the rates of major and trace component variation observed in the three studied suggest that oxidation has been considerably more extensive in the CV chromites than in the other two populations, and probably least prolonged in the Ronda chromian spinels; given their different ages, it also seems likely that the major loss in Al (and, on a lesser scale, Zn) observed in the CV chromite set might be due to more prolonged fluid-peridotite interaction.

Thus, it seems reasonable to consider that selective mobility of Al (±Zn) during oxidation of serpentinite-hosted chromites may be enhanced, not only by interaction with high-pH fluids, but also by the extent of water-rock interaction. Therefore, the present study confirmed that, irrespective of the geological setting, chromite oxidation patterns during host-peridotite serpentinization are essentially similar, with deviations from strict co-linearity mainly due to the specific composition of the interacting fluid (particularly its pH) and most probably to local fluid/rock ratios. Moreover, the extent of fluid-rock interaction is also a fundamental factor that will naturally condition the extent of chromite oxidation and of component depletion.

Even if, due to lack of fluid/rock data for all the studied settings, it has not been possible to quantify the exact influence of this factor in the chromite oxidation rates and in the chemical changes related to the chromite–ferritchromit (−magnetite) transition(s), the conclusions presented above are relevant to the study and interpretation of the metasomatic processes (and intervening fluids) affecting chromite-bearing rocks and chromite-bearing ores, where metal-concentration processes also depend strongly on the same factors, namely, fluid composition, fluid/rock ratios and the extent of fluid-rock interaction.

Supplementary Materials: The following supporting information can be downloaded at: https://www.mdpi.com/article/10.3390/min12101300/s1, Table S1. Supplementary Data File: "Chromite Composition—complete EMP data sets for the MAR mag-nesiochromites, CV chromites and Ronda chromian spinels".

Author Contributions: Conceptualization, I.R.d.C.; methodology, I.R.d.C. and F.J.A.S.B.; investigation, I.R.d.C. and F.J.A.S.B.; writing—original draft preparation, I.R.d.C.; writing—review and editing, I.R.d.C. and F.J.A.S.B.; funding acquisition, F.J.A.S.B. All authors have read and agreed to the published version of the manuscript.

Funding: This work was funded by the Portuguese Fundação para a Ciência e a Tecnologia (FCT) I.P./MCTES through national funds (PIDDAC)—UIDB/500019/2020.

Data Availability Statement: Data are available in PDF format in the Supplementary Material section.

Acknowledgments: Analytical data presented and discussed in this study was based on previous research, through FCT—Fundação para a Ciência e a Tecnologia project grants LIOFLUX-Praxis XXI and SEAHMA-PDCTM (for the MAR data), and ORVITER-PTDC/AAG-MAA/2891/2012 (for the CV data). The first author gratefully acknowledges the invaluable help of: Alberto Verde and Cyntia Mourão (GeoFCUL, ULisboa), who prepared the polished thin-sections used for petrographic and mineralogical study; Octávio Chaveiro and Pedro Celestino Rodrigues, operating the EMP facilities at ULisboa; Fernanda Guimarães, operating the EMP facility at LNEG (S. Mamede de Infesta, Porto); and Ivo Martins for his help with submission procedures.

Conflicts of Interest: The authors declare no conflict of interest. The funders had no role in the design of the study; in the collection, analyses, or interpretation of data; in the writing of the manuscript, or in the decision to publish the results.

Appendix A

Table A1. Representative and average EMP data and structural formulae of chromites from the MAR (Rainbow and Saldanha sites), Cabeço de Vide (Alter do Chão Massif, Portugal) and Ronda (SW Spain) serpentinites. The selected representative analyses show minimum and maximum oxidation effects. Cations per formula unit were estimated on a basis of four oxygen atoms and assuming full occupancy of the B (trivalent cation) position.

Location	**MID-ATLANTIC RIDGE**								**CABEÇO DE VIDE**								**RONDA**							
	Grain 1		Grain 2		Average 32 grains (st.dev.)				Grain 1		Grain 2		Average 36 grains (st.dev.)				Grain 1		Grain 2		Average 25 grains (st.dev.)			
	(core)	(rim)	(core)	(rim)	Cores		Rims		(core)	(rim)	(core)	(rim)	Cores		Rims		(core)	(rim)	(core)	(rim)	Cores		Rims	
TiO_2	0.21	0.21	0.30	0.33	0.16	(0.15)	0.25	(0.18)	1.79	3.39	1.62	2.08	2.18	(1.72)	2.13	(1.70)	0.00	0.04	0.04	0.06	0.22	(0.45)	0.19	(0.43)
Cr_2O_3	49.35	47.01	47.40	44.08	42.60	(3.32)	40.88	(9.60)	36.97	34.48	35.35	31.25	33.15	(5.30)	30.18	(7.40)	12.44	14.19	37.13	52.04	28.38	(10.00)	28.89	(13.27)
Al_2O_3	19.80	19.61	19.71	7.05	23.21	(4.88)	16.39	(8.59)	17.69	6.50	21.76	3.46	17.76	(6.21)	2.30	(1.56)	55.57	52.09	31.33	16.17	38.49	(8.81)	33.19	(13.71)
V_2O_3	0.22	0.18	0.18	0.22	0.16	(0.07)	0.18	(0.12)	n.d.	n.d.	n.d.	n.d.	n.d.		n.d.		0.07	0.03	0.13	0.12	0.19	(0.14)	0.18	(0.17)
FeO	16.49	18.79	20.58	39.49	20.53	(5.40)	30.05	(15.72)	38.44	49.43	31.13	58.44	39.85	(10.23)	58.52	(9.43)	11.04	10.79	14.68	18.93	15.88	(3.61)	21.76	(19.89)
MnO	0.35	0.36	0.39	0.60	0.30	(0.13)	0.36	(0.23)	0.69	0.70	0.40	0.74	0.74	(0.21)	0.87	(0.30)	0.12	0.17	0.25	0.36	0.21	(0.06)	0.22	(0.09)
MgO	12.40	11.17	10.92	3.88	11.63	(2.05)	8.43	(3.74)	3.96	2.90	9.19	1.37	4.54	(2.26)	1.38	(0.72)	19.39	19.11	15.48	11.84	15.84	(1.71)	14.16	(4.55)
NiO	0.07	0.09	0.08	0.09	0.09	(0.04)	0.11	(0.09)	0.18	0.16	0.19	0.08	0.15	(0.07)	0.13	(0.08)	n.d.	n.d.	n.d.	n.d.	n.d.		n.d.	
ZnO	0.15	0.17	0.25	0.31	0.20	(0.11)	0.23	(0.12)	0.54	0.23	0.16	0.64	0.81	(0.50)	0.43	(0.18)	n.d.	n.d.	n.d.	n.d.	n.d.		n.d.	
Total	99.03	97.60	99.81	96.05	98.88	(1.34)	96.88	(3.77)	100.34	97.94	99.81	98.07	99.23	(2.49)	95.97	(1.31)	98.63	96.41	99.04	99.52	99.20	(0.85)	98.59	(2.20)
Cations estimated assuming 4 oxygen atoms and 2 trivalent cations per formula unit																								
Ti	0.005	0.005	0.007	0.009	0.004		0.007		0.044	0.090	0.038	0.056	0.054		0.059		0.000	0.001	0.001	0.002	0.005		0.004	
Cr	1.226	1.192	1.180	1.255	1.051		1.124		0.960	0.957	0.876	0.891	0.860		0.881		0.260	0.305	0.863	1.311	0.648		0.672	
Al	0.733	0.741	0.732	0.299	0.846		0.649		0.685	0.269	0.803	0.147	0.678		0.099		1.729	1.669	1.086	0.607	1.284		1.119	
V	0.005	0.005	0.005	0.006	0.004		0.005		-	-	-	-	-		-		0.001	0.001	0.003	0.003	0.004		0.004	
Fe^{3+}	0.031	0.057	0.076	0.431	0.094		0.216		0.311	0.684	0.283	0.906	0.408		0.960		0.010	0.024	0.046	0.077	0.059		0.200	
Total $^{3+}$	2.000	2.000	2.000	2.000	2.000		2.000		2.000	2.000	2.000	2.000	2.000		2.000		2.000	2.000	2.000	2.000	2.000		1.999	
Fe^{2+}	0.402	0.447	0.466	0.758	0.446		0.557		0.745	0.768	0.533	0.856	0.709		0.852		0.234	0.221	0.315	0.427	0.321		0.385	
Mn	0.009	0.010	0.011	0.018	0.008		0.011		0.019	0.021	0.011	0.023	0.021		0.027		0.003	0.004	0.006	0.010	0.005		0.005	
Mg	0.581	0.534	0.513	0.208	0.537		0.421		0.194	0.152	0.429	0.074	0.219		0.076		0.763	0.775	0.679	0.562	0.672		0.609	
Ni	0.002	0.002	0.002	0.003	0.002		0.003		0.005	0.005	0.005	0.002	0.004		0.004		-	-	-	-	-		-	
Zn	0.003	0.004	0.006	0.008	0.005		0.006		0.013	0.006	0.004	0.017	0.020		0.012		-	-	-	-	-		-	
Total $^{2+}$	0.998	0.997	0.996	0.996	0.998		0.997		0.978	0.955	0.981	0.972	0.973		0.971		1.000	1.000	1.000	1.000	0.998		0.999	
Total cations	2.998	2.997	2.996	2.996	2.998		2.997		2.978	2.955	2.981	2.972	2.973		2.971		3.000	3.000	3.000	2.999	2.998		2.998	
$Fe^{3+}/(Fe^{2+} + Fe^{3+})$	0.07	0.11	0.14	0.36	0.15		0.23		0.29	0.47	0.35	0.51	0.337		0.52		0.039	0.098	0.13	0.15	0.14		0.19	
$Mg/(Mg + Fe^{2+})$	0.59	0.54	0.52	0.22	0.55		0.43		0.21	0.17	0.45	0.08	0.234		0.08		0.77	0.78	0.68	0.57	0.68		0.61	
Al + Cr	1.96	1.93	1.91	1.55	1.90		1.77		1.64	1.23	1.68	1.04	1.538		0.98		1.99	1.97	1.95	1.92	1.93		1.79	
#Cr	0.63	0.62	0.62	0.81	0.56		0.65		0.58	0.78	0.52	0.86	0.583		0.91		0.13	0.15	0.44	0.68	0.34		0.42	
#Fe	0.41	0.46	0.48	0.78	0.45		0.57		0.79	0.83	0.55	0.92	0.766		0.92		0.23	0.22	0.32	0.43	0.32		0.39	
#Cr/#Fe	1.53	1.35	1.30	1.03	1.24		1.16		0.74	0.93	0.94	0.93	0.764		0.99		0.56	0.70	1.40	1.58	1.05		1.11	

References

1. Deer, W.A.; Howie, R.A.; Zussman, J. *An Introduction to Rock-Forming Minerals*, 2nd ed.; Longman: Hong-Kong, China, 1992.
2. Bosi, F.; Biagioni, C.; Pasero, M. Nomenclature and classification of the spinel supergroup. *Eur. J. Mineral.* **2019**, *31*, 183–192. [CrossRef]
3. Beeson, M.H.; Jackson, E.D. Chemical composition of altered chromites from the Stillwater Complex, Montana. *Amer. Min.* **1969**, *54*, 1084–1100.
4. Ulmer, G.C. Alteration of chromite during serpentinization in the Pennsylvania-Maryland District. *Amer. Min.* **1974**, *59*, 1236–1241.
5. Onyeagocha, A.C. Alteration of chromite from the Twin Sisters dunite, Washington. *Amer. Min.* **1974**, *59*, 608–612.
6. Hoffman, M.A.; Walker, D. Textural and chemical variations of olivine and chrome spinel in the East Dover ultramafic bodies, south-central Vermont. *Geol. Soc. Am. Bull.* **1978**, *89*, 699–710. [CrossRef]
7. Georgiou, E.; Xenophontos, C. Chromite occurrences and associated plutonic rocks in the Akapnou Forest. In *Ophiolites Oceanic Crustal Analogues: Proceedings of the Symposium "Troodos 1987"*; Geological Survey Dept.: Nicosia, Cyprus, 1990; pp. 585–592.
8. Kimball, K.L. Effects of hydrothermal alteration on the compositions of chromian spinels. *Contrib. Mineral. Petrol.* **1990**, *105*, 337–346. [CrossRef]
9. Roeder, P.L. Chromite: From the fiery rain of chondrules to the Kilauea Iki lava lake. *Can. Min.* **1994**, *32*, 729–746.
10. Kamenetsky, V.S.; Crawford, A.J.; Meffre, S. Factors controlling chemistry of magmatic spinel: An empirical study of associated olivine, Cr-spinel and melt inclusions from primitive rocks. *J. Petrol.* **2001**, *42*, 655–671. [CrossRef]
11. Mellini, M.; Rumori, C.; Viti, C. Hydrothermally reset magmatic spinels in retrograde serpentinites: Formation of «ferritchromit» rims and chlorite aureoles. *Contrib. Mineral. Petrol.* **2005**, *149*, 266–275. [CrossRef]
12. Gervilla, F.; Asta, M.P.; Fanlo, I.; Grolimund, D.; Ferreira-Sánchez, D.; Samson, V.A.; Hunziker, D.; Colás, V.; González-Jiménez, J.M.; Kerestedjian, T.N.; et al. Diffusion pathways of Fe^{2+} and Fe^{3+} during the formation of ferrian chromite: A μXanes study. *Contrib. Mineral. Petrol.* **2019**, *174*, 65. [CrossRef]
13. Ribeiro da Costa, I. Serpentinization on the Mid-Atlantic Ridge: The Rainbow, Saldanha and Menez Hom Sites. PhD Thesis, Lisbon University, Lisbon, Portugal, 2005.
14. Ribeiro da Costa, I.; Barriga, F.J.A.S. The upper mantle beneath the Mid-Atlantic Ridge in the Azores sector. *Comun. Geol.* **2010**, *97*, 23–34.
15. Ribeiro da Costa, I.; Wicks, F.J.; Barriga, F.J.A.S. Serpentinization at the Rainbow and Saldanha sites, Mid-Atlantic Ridge: Mineralogical, geochemical and isotopic features. *Can. Min.* **2019**, *57*, 677–706. [CrossRef]
16. Detrick, R.S.; White, R.S.; Purdy, G.M. Crustal structure of North Atlantic fracture zones. *Rev. Geophys.* **1993**, *31*, 439–458. [CrossRef]
17. German, C.R.; Parson, L.M. The HEAT Scientific Team. Hydrothermal exploration at the Azores Triple Junction: Tectonic control of venting at slow spreading ridges? *Earth Planet. Sci. Lett.* **1996**, *138*, 93–104. [CrossRef]
18. Barriga, F.J.A.S.; Costa, I.M.A.; Relvas, J.M.R.S.; Ribeiro, A.; Fouquet, Y.; Ondréas, H.; Parson, L. The FLORES Scientific Party. The Rainbow serpentinites and serpentinite-sulphide stockwork (Mid-Atlantic Ridge, AMAR segment): A preliminary report of the FLORES results. *Eos Trans. Am. Geophys. Union* **1997**, *78*, F832–F833.
19. Fouquet, Y.; Charlou, J.L.; Ondréas, H.; Radford-Knoery, J.; Donval, J.P.; Douville, E.; Appriou, R.; Cambon, P.; Pellé, H.; Landuré, J.Y.; et al. Discovery and first submersible investigations on the Rainbow hydrothermal field on the MAR (36°14′ N). *EOS Trans. Am. Geophys. Union* **1997**, *78*, F832.
20. Barriga, F.J.A.S.; Fouquet, Y.; Almeida, A.; Biscoito, M.; Charlou, J.L.; Costa, R.L.P.; Dias, A.; Marques, A.; Miranda, J.M.; Olu, K.; et al. Preliminary results of the Saldanha mission (FAMOUS segment of the MAR 36°30′ N). *Geophys. Res. Abstr.* **1999**, *1*.
21. Parson, L.; Gràcia, E.; Coller, D.; German, C.; Needham, D. Second-order segmentation; the relationship between volcanism and tectonism at the MAR, 38° N–35°40′ N. *Earth Planet. Sci. Lett.* **2000**, *178*, 231–251. [CrossRef]
22. Gràcia, E.; Charlou, J.L.; Radford-Knoery, J.; Parson, L.M. Non-transform offsets along the Mid-Atlantic Ridge south of the Azores (38° N–34° N): Ultramafic exposures and hosting of hydrothermal events. *Earth Planet. Sci. Lett.* **2000**, *177*, 89–103. [CrossRef]
23. Miranda, J.M.; Silva, P.F.; Lourenço, N.; Henry, B.; Costa, R.; SALDANHA Team. Study of the Saldanha massif (MAR, 36°34′ N): Constraints from rock magnetic and geophysical data. *Mar. Geophys. Res.* **2003**, *23*, 299–318. [CrossRef]
24. Francis, T.J.G. Serpentinization faults and their role in the tectonics of slow spreading ridges. *J. Geophys. Res.* **1981**, *86*, 11616–11622. [CrossRef]
25. Mével, C.; Cannat, M.; Gente, P.; Marion, E.; Auzende, J.M.; Karson, J.A. Emplacement of deep crustal and mantle rocks on the west median valley wall of the MARK area (MAR, 23° N). *Tectonophysics* **1991**, *190*, 31–53. [CrossRef]
26. Detrick, R.S.; Needham, H.D.; Renard, V. Gravity anomalies and crustal thickness variations along the Mid-Atlantic Ridge betweeen 33° N and 40° N. *J. Geophys. Res.* **1995**, *100*, 3767–3787. [CrossRef]
27. Tucholke, B.E.; Lin, J. A geological model for the structure of ridge segments in slow-spreading ocean crust. *J. Geophys. Res.* **1994**, *99-B*, 11937–11958. [CrossRef]
28. Cannat, M.; Mével, C.; Maia, M.; Deplus, C.; Durand, C.; Gente, P.; Agrinier, P.; Belarouchi, A.; Dubuisson, G.; Humler, E.; et al. Thin crust, ultramafic exposures, and rugged faulting patterns at the Mid-Atlantic Ridge (22°–24° N). *Geology* **1995**, *23*, 49–52. [CrossRef]
29. Escartín, J.; Hirth, G.; Evans, B. Effects of serpentinization on the lithosphere strength and the style of normal faulting at slow-spreading ridges. *Earth Planet. Sci. Lett.* **1997**, *151*, 181–189. [CrossRef]

30. White, R.S.; Minshull, T.A.; Bickle, M.J.; Robinson, C.J. Melt generation at very slow-spreading oceanic ridges: Constraints from geochemical and geophysical data. *J. Petrol.* **2001**, *42*, 1171–1196. [CrossRef]
31. Gonçalves, F.; Fernandes, A.P. *Notícia Explicativa da Folha 32B: Portalegre, Carta Geológica de Portugal 1/50,000*; Serviços Geológicos de Portugal: Lisboa, Portugal, 1973.
32. Canilho, M.H. Complexo plutónico básico e ultrabásico de Alter do Chão. *Bol. Soc. Geol. Port.* **1973**, *18*, 155–170.
33. Ribeiro da Costa, I. Estudo do Processo de Rodingitização das Rochas Gabróicas de Cabeço de Vide Associado à Serpentinização dos Ultrabasitos Encaixantes. Graduation Thesis, Lisbon University, Lisbon, Portugal, 1985.
34. Lopes, J.M.C.C.A. Petrologia e Geoquímica de Complexos Plutónicosdo NE Alentejano (ZOM), Portugal Central: Província Alcalina e Maciço de Campo Maior. Ph.D. Thesis, University of Évora, Évora, Portugal, 2004.
35. Torné, M.; Banda, E.; García-Dueñas, V.; Balanya, J.C. Mantle lithosphere bodies in the Alboran crustal domain (Ronda peridotites Betic-Rif orogenic belt). *Earth Planet. Sci. Lett.* **1992**, *110*, 163–171. [CrossRef]
36. Tubía, J.M.; Cuevas, J.; Navarro-Villa, F.; Alvarez, F.; Aldaya, F. Tectonic evolution of the Alpujárride Complex (Betic Cordilleras, southern Spain). *J. Struct. Geol.* **1992**, *14*, 193–203. [CrossRef]
37. Menzies, A.M.; Dupuy, C. Orogenic massifs: Protolith, process and provenance. *J. Petrol.* **1991**, 1–16. [CrossRef]
38. Thayer, T.P. Some critical differences between alpine-type and stratiform peridotite-gabbro complexes. *Int. Geol. Congr. 21th Sess. Cph.* **1960**, *13*, 247–259.
39. Nicolas, A.; Jackson, E.D. Répartition en deux provinces des péridotites des chaînes alpines longeant la Méditerranée. *Bull. Suisse Miner. Petrol.* **1972**, *52*, 397–495.
40. Obata, M.; Suen, C.J.; Dickey, J.S. The origin of mafic layers in the Ronda high-temperature peridotite intrusion, S. Sain: An evidence of partial fusion and fractional crystallization in the upper mantle. *Colloq. Int. CNRS* **1980**, *275*, 257–268.
41. Tubía, J.M.; Cuevas, J.; Gil Ibarguchi, J.I. Sequential development of the metamorphic aureole beneath the Ronda peridotites and its bearing on the tectonic evolution of the Betic Cordillera. *Tectonophysics* **1997**, *279*, 227–252. [CrossRef]
42. Obata, M. The Ronda peridotite: Granet-, spinel- and plagioclase-lherzolite facies and the P-T trajectories of a high-temperature mantle intrusion. *J. Petrol.* **1980**, *21*, 533–572.
43. Darot, M. Cinématique de l'extrusion, à partir du manteaux, des péridotites de la Sierra Bermeja (Seranía de Ronda, Espagne). *C. Rend. Acad. Sc. Paris* **1974**, *278*, 1673–1676.
44. Lundeen, M.T. Emplacement of the Ronda peridotite, Sierra Bermeja, Spain. *Bull. Geol. Soc. Am.* **1978**, *89*, 172–180. [CrossRef]
45. Platt, J.P.; Argles, T.W.; Carter, A.; Kelley, S.P.; Whitehouse, M.J.; Lonergan, L. Exhumation of the Ronda peridotite and its crustal envelope: Constraints from thermal modeling of a P-T-time array. *J. Geol. Soc. London* **2003**, *160*, 655–676. [CrossRef]
46. Casas, A.; Carbó, A. Deep structure of the Betic Cordillera derived from the interpretatin of a complete Bouger anomaly map. *J. Geod.* **1990**, *12*, 137–147. [CrossRef]
47. Balanyá, J.C. Estructura del Domínio de Alborán en la del Arco de Gibraltar. Ph.D. Thesis, Granada University, Granada, Spain, 1991.
48. Van der Wal, D. Deformation processes in mantle peridotites with emphasis on the Ronda peridotite of SW Spain. Ph.D. Thesis, Utrecht Universit, Utrecht, Holland, 1993.
49. Tubía, J.M. The Ronda peridotites (Los Reales nappe): An example of the relationship between lithospheric thickening by oblique tectonics and late extensional deformation within the Betic Cordillera (Spain). *Tectonophysics* **1994**, *138*, 381–398. [CrossRef]
50. Platt, J.P.; Anczkiewicz, R.; Soto, J.-I.; Kelley, S.P.; Thirlwall, M. Early Miocene continental subduction and rapid exhumation in the western Mediterranean. *Geology* **2006**, *34*, 981. [CrossRef]
51. Hidas, K.; Booth-Rea, G.; Garrido, C.J.; Martínez-Martínez, J.M.; Padrón-Navarta, J.A.; Konc, Z.; Giaconia, F.; Frets, E.; Marchesi, C. Backarc basin inversion and subcontinental mantle emplacement in the crust: Kilometre-scale folding and shearing at the base of the proto-Alborán lithospheric mantle (Betic Cordillera, southern Spain). *J. Geol. Soc.* **2013**, *170*, 47–55. [CrossRef]
52. Giampouras, M.; Garrido, C.J.; Zwicker, J.; Vadillo, I.; Smrzka, D.; Bach, W.; Peckmann, J.; Jimenez, P.; Benavente, J.; García-Ruiz, J.M. Geochemistry and mineralogy of serpentinization-driven hyperalkaline springs in the Ronda peridotites. *Lithos* **2019**, *350–351*, 105215. [CrossRef]
53. Figueiras, J.; Lisbon University, Lisbon, Portugal; Mateus, A.; Lisbon University, Lisbon, Portugal. Personal Communication, 2005.
54. Waerenborgh, J.C.; Figueiras, J.; Mateus, A.; Gonçalves, M. ^{57}Fe Mössbauer spectroscopy study of the correlation between Fe^{3+} contente and the magnetic properties of natural Cr-spinels. *Eur. J. Mineral.* **2002**, *14*, 437–446. [CrossRef]
55. Gresens, J.L. Composition—volume relationships of metasomatism. *Chem. Geol.* **1967**, *2*, 47–65. [CrossRef]
56. Ribeiro da Costa, I.; Jesus, A.P.; Munhá, J.M.; Barriga, F.J.A.S. Oxygen barometry of upper mantle beneath the Azores sector of the Mid-Atlantic Ridge. *Geochim. Cosmochim. Acta* **2006**, *70 (18S)*, A124. [CrossRef]
57. Dick, H.B.; Bullen, T. Chromian spinel as a petrogenetic indicator in abyssal and alpine-type peridotites and spatially associated lavas. *Contrib. Mineral. Petrol.* **1984**, *86*, 54–76. [CrossRef]
58. Paulick, H.; Bach, W.; Godard, M.; De Hoog JC, M.; Suhr, G.; Harvey, J. Geochemistry of abyssal peridotites (Mid-Atlantic Ridge, 15°20′ N, ODP Leg 209): Implications for fluid/rock interaction in slow spreading environments. *Chem. Geol.* **2006**, *234*, 179–210. [CrossRef]
59. Sverjensky, D.A.; Shock, E.L.; Helgeson, H.C. Prediction of the thermodynamic properties of aqueous metal complexes to 1000 °C and 5 kb. *Geochim. Cosmochim. Acta* **1997**, *61*, 13591412. [CrossRef]

60. Wicks, F.J. Lizardite and its parent enstatite: A study by X-ray diffraction and transmission electron microscopy. *Can. Min.* **1986**, *24*, 775–788.
61. Malvoisin, B.; Brunet, F.; Carlut, J.; Rouméjon, S.; Cannat, M. Serpentinization of oceanic peridotites: 2. Kinetics and processes of San Carlos olivine hydrothermal alteration. *J. Geophys. Res.* **2012**, *117*, B04102. [CrossRef]
62. Klein, F.; Bach, W.; Humphris, S.E.; Kahl, W.-A.; Jöns, N.; Moskowitz, B.; Berquó, T. Magnetite in seafloor serpentinite—Some like it hot. *Geology* **2014**, *42*, 135–138. [CrossRef]
63. Wenner, D.B.; Taylor, H.P., Jr. Oxygen and hydrogen isotope studies of serpentinization of ultramafic rocks on oceanic environments and continental ophiolite complexes. *Am. J. Sci.* **1973**, *273*, 207–239. [CrossRef]
64. Sakai, R.; Kusakabe, M.; Noto, M.; Ishii, T. Origin of waters responsible for serpentinization of the Izu-Ogasawara-Mariana forearc seamounts in view of hydrogen and oxygen isotope ratios. *Earth Planet. Sci. Lett.* **1990**, *100*, 291–303. [CrossRef]
65. Azimov, P.Y.; Bushmin, S.A. Solubility of Minerals of Metamorphic and Metasomatic Rocks in Hydrothermal Solutions of Varying Acidity: Thermodynamic Modeling at 400–800 °C and 1–5 kbar. *Geochem. Int.* **2007**, *45*, 1210–1234. [CrossRef]
66. Portugal Ferreira, M.; Lopo Mendonça, J. Enquadramento geológico e hidrogeológico das nacentes de água minero-medicinal de Cabeço de Vide. In *Livro de Homenagem a Carlos Romariz*; Secção de Geologia Económica e Aplicada, Ed.; Departamento de Geologia, Universidade de Lisboa: Lisboa, Portugal, 1990; pp. 151–173.
67. Marques, J.M.; Carreira, P.M.; Carvalho, M.R.; Matias, M.J.; Goff, F.E.; Basto, M.J.; Graça, R.C.; Aires-Barros, L.; Rocha, L. Origins of high pH mineral waters from ultramafic rocks, Central Portugal. *Appl. Geochem.* **2008**, *23*, 3278–3289. [CrossRef]
68. Barnes, I.; LaMarche, V.C., Jr.; Himmelberg, G. Geochemical evidence of present-day serpentinization. *Science* **1967**, *156*, 830–832. [CrossRef]
69. Acosta, A.; Pereira, M.D.; Shaw, D.M.; Bea, F. Serpentinización de la peridotita de Ronda (Cordillera Bética) por la interacción con fluidos ricos en volatiles: Comportamiento del B. *Rev. Soc. Geol. España* **1997**, *10*, 301–308.
70. Palmer, D.A.; Wesolowski, D.; Bénézeth, P. The Aqueous Chemistry of Aluminium in a New Approach to High-Temperature Solubility Measurements. 1996. Available online: digital.library.unt.edu (accessed on 16 August 2022).
71. Zaraiskii, G.P. On the Differential Mobility of Components during Experimental Diffusion Metasomatism. In *Problems of Physicochemical Petrology (State of Fluid and Solutions, Metasomatism, Ore Formation)*; Nauka: Moscow, Russian, 1979; Volume 2, pp. 118–144. (In Russian)
72. Martin, B.; Fyfe, W.S. Some experimental and theoretical observationson the kinetics of hydration reactions with particular reference to serpentinization. *Chem. Geol.* **1970**, *6*, 185–202. [CrossRef]
73. Macdonald, A.H.; Fyfe, W.S. Rate of serpentinization in seafloor environments. *Tectonophysics* **1985**, *116*, 123–135. [CrossRef]
74. Watson, E.B.; Brenan, J.M. Fluids in the lithosphere, 1. Experimentally-determined wetting characteristics of CO_2-H_2O fluids and their implications for fluid transport, host-rock physical properties, and fluid inclusion formation. *Earth Planet. Sci. Lett.* **1987**, *85*, 497–515. [CrossRef]
75. Macfarlane, N.D.; Mossman, D.J. The opaque minerals and economic geology of the Nemeiben Ultramafic Complex, Saskatchewan, Canada. *Mineral. Deposita* **1981**, *16*, 409–424. [CrossRef]
76. Tesalina, S.G.; Nimis, P.; Augé, T.; Zaykov, V.V. Origin of chromite in mafic-ultramafic-hosted massive sulfides from the Main Uralian Fault, South Urals, Russia. *Lithos* **2003**, *70*, 39–59. [CrossRef]
77. Barnes, S.J.; Tang, Z.-L. Chrome spinels from the Jinchuan Ni-Cu sulfide deposit, Gansu Province, People's Republic of China. *Econ. Geol.* **1999**, *94*, 343–356. [CrossRef]